


2009-01-01

# Experimental study of the response of Semiconductor Detectors for EDXRF Analysis.

Sunil Kumar Valaparla

*University of Texas at El Paso*, skvalaparla@miners.utep.edu

Follow this and additional works at: [https://digitalcommons.utep.edu/open\\_etd](https://digitalcommons.utep.edu/open_etd)

 Part of the [Atomic, Molecular and Optical Physics Commons](#), [Materials Science and Engineering Commons](#), and the [Mechanics of Materials Commons](#)

---

## Recommended Citation

Valaparla, Sunil Kumar, "Experimental study of the response of Semiconductor Detectors for EDXRF Analysis." (2009). *Open Access Theses & Dissertations*. 375.

[https://digitalcommons.utep.edu/open\\_etd/375](https://digitalcommons.utep.edu/open_etd/375)

This is brought to you for free and open access by DigitalCommons@UTEP. It has been accepted for inclusion in Open Access Theses & Dissertations by an authorized administrator of DigitalCommons@UTEP. For more information, please contact [lweber@utep.edu](mailto:lweber@utep.edu).

EXPERIMENTAL STUDY OF THE RESPONSE OF SEMICONDUCTOR  
DETECTORS FOR EDXRF ANALYSIS.

SUNIL K VALAPARLA

Department of Physics

APPROVED

---

Miguel Castro-Colín, Ph.D., Chair

---

Jorge A. López, Ph.D.

---

Ramana V. Chintalapalle, Ph.D.

---

Tunna Baruah, Ph.D.

---

Patricia D. Witherspoon, Ph.D.  
Dean of the Graduate School

Copyright ©

by

Sunil K Valaparla

2009

*Trust in the Lord with all your heart, and lean not on your own understanding; in all your ways acknowledge Him, and He shall direct your paths.*

*Proverbs 3 : 5-6*

EXPERIMENTAL STUDY OF THE RESPONSE OF SEMICONDUCTOR  
DETECTORS FOR EDXRF ANALYSIS.

by

SUNIL K VALAPARLA

THESIS

Presented to the Faculty of the Graduate School of

The University of Texas at El Paso

in Partial Fulfillment

of the Requirements

for the Degree of

MASTER OF SCIENCE

Department of Physics

THE UNIVERSITY OF TEXAS AT EL PASO

August 2009

## Acknowledgments

I am indebted to many people who have contributed to the work of this thesis. First and foremost I want to thank Dr.M. Castro-Colin, my advisor, for providing me the opportunity to work and complete this thesis under his direction.

I am grateful to Dr.J. A. López for the generous assistance and guidance during my graduate studies.

My sincere gratitude is extended to the members of my committee Dr.J. A. López, Dr.T. Baruah, and Dr.C. V. Ramana.

I am also grateful for the help, support and friendship from my labmates and other graduate students, including Felipe Tovar, Miguel Bencomo and Enrique Diaz. I would also like to thank Ed Bustamante, the machinist for helping me in preparing the equipment for my experiment.

Finally, I would like to thank my dad Dr.V. Veeraiah and my family members for their love, encouragement, support and understanding.

*August, 2009*

V. Sunil Kumar

## Abstract

This present work relates to the study and characterization of the response function of an energy-dispersive x-ray spectrometer. The problems of energy, efficiency and resolution calibration of the system operating in the energy (5-60 keV) range are discussed. We present the operation characteristics of the portable pyro-electric x-ray generator (COOL-X) and the application of the calibrated response spectrum in the elemental analysis using X-ray Fluorescence (XRF). Use of COOL-X as a source of exciting radiation in combination with high resolution semiconductor detectors applied to XRF presents a practical advantage due to the price and small form factor of the components.

The detectors and the COOL-X used in the present study are produced by Amptek. We study the response of the Si(Li)-Pin XR-100CR semiconductor detector to low energy photons. The photopeak efficiency was determined experimentally by using radioisotopes  $^{55}\text{Fe}$ ,  $^{241}\text{Am}$ ,  $^{137}\text{Cs}$  and  $^{133}\text{Ba}$  and compared against a theoretical efficiency curve. The efficiency for  $\gamma$  photons resulting from the decay of the radioactive sources and that of x-rays, was obtained from direct measurements. The response characteristics of CdTe XR-100T detector and the efficiency calculations are performed using  $^{55}\text{Fe}$ ,  $^{241}\text{Am}$ , and  $^{133}\text{Ba}$ . Escape events originated in this detector are observed and discussed. The com-

parison between the detectors and the advantages and disadvantages for XRF are described, together with a discussion of suggested features or expected complications that may arise given certain parameters of the detectors. Given the working conditions of the detectors at hand, one outcome has been that, for the low energies, below 25 keV, the Si(Li)-PIN detector has better energy resolution, lower background counts. For higher energy x-rays, above 25 keV, CdTe has better stopping power, which improves its efficiency. The former, are general considerations made by the manufacturer [13] that are here confirmed.

Analysis of energies and intensities of fluorescent x-rays emitted from a given material when atoms are bombarded with electrons or photons has been successfully used for non-destructive elemental analysis. We present a brief analysis of elemental content carried out by means of a pyro-electric generator in combination with a CdTe and a Si(Li)-Pin energy dispersive detectors. The setup presented here can be easily assembled in an average laboratory to observe the effect of X-rays as they interact with matter to yield a characteristic fingerprint, a phenomenon that directly relates to atomic theory. In the present case three pieces of metal whose elemental content has been characterized were analyzed and their elemental content shown. Additionally we performed the elemental analysis using a Si(Li)-Pin detector on standard ref-



erence materials and their elemental energy lines have been identified. These results have been compared with those obtained from an X-ray analysis system XMET 3000 TXV+, also based on a Si-Pin detector but with a Silver X-ray excitation source. Such a system has been used to estimate the elemental mass fraction (%).

# Contents

<b>Acknowledgments</b>	<b>iv</b>
<b>Abstract</b>	<b>v</b>
<b>List of Figures</b>	<b>xi</b>
<b>List of Tables</b>	<b>xviii</b>
<b>1 Introduction</b>	<b>1</b>
1.1 Interaction of Radiation with matter . . . . .	1
1.2 Mechanisms of Gamma Ray Interactions . . . . .	7
1.3 X-Ray Physics . . . . .	10
1.3.1 Continuous and Characteristic Radiation . . . . .	11
1.3.2 X-ray Spectra . . . . .	11
1.4 Attenuation of Gamma Radiation . . . . .	13

<b>2</b>	<b>Semiconductor Detectors for Spectroscopy</b>	<b>17</b>
2.1	Semiconductors and EM-Radiation Detection . . . . .	18
2.1.1	The band structure of solids . . . . .	18
2.1.2	Creation of charge carriers by gamma radiation . . . . .	20
2.2	Operation of a semiconductor detector . . . . .	23
2.3	Charge collection in Detectors . . . . .	24
2.3.1	Charge collection time . . . . .	24
2.3.2	Trapping of charge carriers . . . . .	26
<b>3</b>	<b>Experimental development</b>	<b>29</b>
3.1	X-ray Generator . . . . .	29
3.1.1	Theory of operation . . . . .	30
3.2	Samples . . . . .	31
3.3	General methodology . . . . .	32
3.4	Si(Li) Pin X-ray Detector (XR-100CR) . . . . .	33
3.4.1	Theory of operation . . . . .	34
3.5	CdTe X-ray and Gamma Ray Detector . . . . .	36
3.5.1	Theory of operation . . . . .	37
3.5.2	Charge trapping in XR-100T CdTe . . . . .	38
3.6	Spectrometer Calibration . . . . .	39

3.6.1	Sources and Reference Data for Calibration . . . . .	39
3.6.2	Energy Calibration . . . . .	40
3.6.3	Peak Width Calibration . . . . .	41
3.6.4	Various methods for Efficiency Calibration . . . . .	43
3.6.5	Importance of Calibration in XRF . . . . .	44
3.6.6	Efficiency Calibration . . . . .	45
3.6.7	Escape Peaks . . . . .	61
3.7	Si-Pin vs CdTe Comparison . . . . .	62
<b>4</b>	<b>XRF measurements</b>	<b>67</b>
4.1	Energy Dispersive XRF Technique . . . . .	67
4.2	Elemental Analysis using a CdTe XR-100T . . . . .	73
4.3	Semi-Quantitative Analysis using a Si(Li) XR-100CR detector .	80
4.4	Comparison of Results with XMET 3000 TXV+ . . . . .	90
<b>5</b>	<b>Conclusion</b>	<b>95</b>
	<b>Bibliography</b>	<b>98</b>
	<b>Appendix</b>	<b>105</b>
<b>A</b>	<b>Technical Specifications</b>	<b>106</b>

A.1	COOL-X . . . . .	106
A.2	XR-100CR . . . . .	109
A.3	XR-100T-CdTe . . . . .	111
A.4	MCA8000A . . . . .	113
A.5	XMET 3000 TXV+ . . . . .	115
<b>B</b>	<b>PyMca Software</b>	<b>117</b>
B.1	Algorithms . . . . .	118
B.1.1	Peak shape model . . . . .	118
B.1.2	FWHM and peak positions . . . . .	118
B.1.3	Element line groups . . . . .	120
B.1.4	Sum and escape peaks . . . . .	122
B.2	Theoretical database . . . . .	123
<b>C</b>	<b>Standard Reference Materials</b>	<b>125</b>
	<b>Curriculum vitae</b>	<b>128</b>

# List of Figures

1.1	The origin of fluorescence . . . . .	5
1.2	Transitions that give rise to various emission lines . . . . .	5
1.3	Phosphorescence . . . . .	6
1.4	Mechanisms of gamma ray interactions [5]. . . . .	8
1.5	Moseley diagrams for the K, L and M series [8] . . . . .	12
1.6	(a) Attenuation of a beam of gamma-rays from a collimated source with intensity $I_0$ ; note that after the attenuator the intensity has a value of $I$ . (b) A lack of collimation of the incident beam implies a more complicated irradiation geometry. . . . .	14
1.7	Attenuation coefficient of materials as a function of gamma energy [4]. . . . .	15
1.8	Comparison of Attenuation coefficient and absorption coefficients of Ge [5] . . . . .	16

2.1	Schematics of the electronic band structures in insulators, metals and semiconductors [11]. . . . .	19
2.2	Basic structure of a semiconductor counter, in this case corresponding to a silicon lithium-drifted crystal, Si(Li) [28]. . . . .	23
2.3	Charge carrier motion in a semiconductor detector . . . . .	25
3.1	Production of X-rays is achieved through the COOL-X Generator. To the left we have the physical COOL-X generator, and to the right a schematic of the x-ray generating system, contained in the nozzle of the actual physical device [13]. . . . .	30
3.2	The spectrum from the COOL-X pyrolithic generator is observed in (a) linear and in (b) log scale. . . . .	31
3.3	Metallic alloys and Standard Reference Materials (SRM) used as samples in the XRF measurements in this thesis. The specific SRMs used are: C2417, 1240cAl, and 1159EM. All SRMs were obtained from the National Institute of Standards and Technology, NIST. . . . .	32
3.4	To the left we can observe the XR-100CR Si-Pin X-ray detector, and to the right a schematic of the internal structure of the detector [13]. . . . .	35

3.5	XR-100T CdTe X-ray detector. . . . .	37
3.6	Schematic diagram of the detector and electronics. . . . .	38
3.7	Energy Calibration of the pyroelectric X-ray source using two characteristic energy lines, Cu $KL_3 = 8.048$ keV and Ta $L_2N_4$ $= 10.895$ keV. As it will be discussed later on, the pyroelectric X-ray source contains a crystal made of $LiTaO_3$ that gives rise to characteristic radiation. . . . .	40
3.8	Estimating FWHM using the area/height ratio. . . . .	41
3.9	Maximum peak height located in two different situations: (a) between two channels and (b) centered about a particular channel.	43
3.10	Linear plot of Intrinsic Full Energy Detection Efficiency vs En- ergy for a Si (Li) Pin Detector. . . . .	47
3.11	Linear plot of interaction probability vs energy for a CdTe de- tector [13]. . . . .	48
3.12	Plot between intrinsic efficiency and photon energy, in log scale, for a XR-100CR detector provided by [13]. . . . .	51
3.13	Spectrum of $^{55}Fe$ obtained from the XR-100CR. . . . .	53
3.14	Spectrum of $^{241}Am$ obtained from the XR-100CR. . . . .	54
3.15	Spectrum of $^{133}Ba$ obtained from the XR-100CR. . . . .	54



3.16	Spectrum of $^{137}\text{Cs}$ obtained from the XR-100CR. . . . .	55
3.17	Comparison of Amptek Model and Theoretical Calculated Efficiency Curves for XR-100CR. . . . .	55
3.18	Comparison of Experimental and Theoretical calculated efficiency points for XR-100CR. . . . .	57
3.19	Spectrum of $^{55}\text{Fe}$ obtained from the XR-100T. . . . .	57
3.20	Spectrum of $^{241}\text{Am}$ obtained from the XR-100T. . . . .	58
3.21	Energy Calibration from $^{241}\text{Am}$ source for XR-100T-CdTe detector.	58
3.22	Spectrum of $^{133}\text{Ba}$ obtained from the XR-100T. . . . .	59
3.23	Energy Calibration from $^{133}\text{Ba}$ source for XR-100T-CdTe detector.	59
3.24	Experimental Efficiency points along with the Amptek Model and Theoretical values for a XR-100T-CdTe detector. . . . .	60
3.25	Comparison of Intrinsic Full Energy Detection Efficiency vs Photon Energy from XR-100CR and XR-100T. . . . .	63
3.26	Comparison of $^{55}\text{Fe}$ Spectrum obtained from XR-100CR and XR-100T. . . . .	64
3.27	Comparison of $^{241}\text{Am}$ Spectrum obtained from XR-100CR and XR-100T. . . . .	66
4.1	Illustration of X-ray Fluorescence . . . . .	68

4.2	Here we show three lines, one referring to the fluorescent yield, which increases with atomic number, another one to the photo-electric mass attenuation coefficient, which decreases with atomic number, and the average K-line energy, which increases with atomic number. . . . .	70
4.3	Experimental Setup . . . . .	74
4.4	Spectrum obtained from the Pyro-electric Generator . . . . .	75
4.5	Spectrum from Ni foil after irradiation for 600s . . . . .	77
4.6	Spectrum from Pb plate irradiated for 600 s . . . . .	78
4.7	Spectrum from Al plate irradiated for 600s . . . . .	79
4.8	X-ray Fluorescence spectrum from 1240c Aluminum Alloy for 500s	81
4.9	Comparison of experimental and fitted data for 1240C. The black triangles represent the experimental data, the red circles represent the fit, and the blue squares indicate the residuals. . . . .	83
4.10	Spectrum from C2417 Lead Base Alloy for 500s . . . . .	85
4.11	Comparison of experimental and fitted data for C2417. The black squares represent the experimental data, the red circles represent the fit, and the blue squares indicate the residuals. . .	86
4.12	Spectrum of 1159 EM Alloy when irradiated for 500s . . . . .	88

4.13	Comparison of experimental and fitted data for 1159. The black squares represent the experimental data, the red circles represent the fit, and the blue squares indicate the residuals. . . . .	88
4.14	To the left we have the XMET 3000 TXV+ with the nozzle pointing vertically upward, and to the right we see the diaphragm pump, used to evacuate the nozzle of the XMET to allow detection of low energy fluorescent peaks. On the right we can also observe the PDA. . . . .	91
4.15	(a) Spectrum of 1240C Al Alloy obtained from XMET for 60 s, and (b) spectrum obtained from XR100CR. . . . .	92
4.16	(a) Spectrum of 1159 EM Alloy obtained from XMET for 60 s, and (b) spectrum obtained from XR100CR. . . . .	93
4.17	(a) Spectrum of C2417 Alloy obtained from XMET for 60 s, and (b) spectrum obtained from XR100CR. . . . .	93
A.1	Cool-X Output flux vs angle [13]. . . . .	107
A.2	Cool-X Controller System [13]. . . . .	107
A.3	Cool-X operation from 2.5 to 4.5 V DC supply [13]. . . . .	108
A.4	Cool-X Mechanical Dimensions [13]. . . . .	108
A.5	Resolution and Peak Shift vs. Count Rate [13]. . . . .	109

A.6	XR-100CR Connection Diagram [13]. . . . .	110
A.7	XR100CR, PX2CR, MCA8000A connection diagram [13]. . . . .	110
A.8	XR100T-CdTe Detector [13]. . . . .	111
A.9	XR100T-CdTe Connection Diagram [13]. . . . .	112
A.10	XR100T-CdTe, PX2T, and MCA8000A Connection Diagram [13].	112
A.11	MCA8000A Pocket multichannel analyzer [13]. . . . .	113
A.12	ADMCA Windows Software showing ROI [13]. . . . .	114
A.13	ADMCA Windows Software showing multiple spectra capability [13]. . . . .	114

# List of Tables

2.1	Parameters of some materials suitable for gamma-ray detectors. For $\epsilon$ the values indicated are given at 77K for Ge and 300K otherwise [11]. . . . .	22
3.1	Characteristics of radioactive sources used for calibration. . . . .	52
3.2	Parameters used for Detector Calibration provided by Amptek. . . . .	53
3.3	Experimental Efficiency results from XR-100CR. . . . .	56
3.4	Experimental Efficiency results from XR-100T. . . . .	60
3.5	Resolution (eV FWHM) Characteristics . . . . .	65
4.1	Emission energies of some metals [44] . . . . .	69
4.2	Results from irradiation of metallic samples. . . . .	79
4.3	Identification of peaks in 1240C Al alloy 3004 . . . . .	82
4.4	Relative Concentrations of 1240C Al Alloy 3004 . . . . .	83
4.5	Identification of peaks in C2417 Pb Alloy . . . . .	86

4.6	Relative Concentrations of C2417 Pb base Alloy . . . . .	87
4.7	Identification of peaks in 1159 EM Alloy . . . . .	89
4.8	Relative Concentrations of 1159 EM Alloy. . . . .	90
4.9	Comparison of mass fraction values for 1240C Al Alloy 3004. . .	94
4.10	Comparison of mass fraction values for 1159 EM Alloy 3004 . .	94
4.11	Comparison of mass fraction values for C2417 Pb Alloy 3004 . .	94
A.1	COOL-X technical specifications. . . . .	106
A.2	XR-100CR technical specifications. . . . .	109
A.3	XR-100T-CdTe Specifications. . . . .	111
A.4	XMET 3000 TXV+ Specifications. . . . .	116
C.1	SRM Specifications. . . . .	125
C.2	Certified Values for SRM 1240c Aluminum Alloy 3004. . . . .	126
C.3	Certified Values for SRM 1159 EM Alloy. . . . .	126
C.4	Certified Values for SRM C2417 Lead base Alloy. . . . .	127

# Chapter 1

## Introduction

In order to study the principles and the calibration techniques which are discussed in this thesis, a general background will be introduced, consisting of solid state detectors and radiation, especially X-rays and gamma rays and the interaction mechanisms between radiation and matter.

### 1.1 Interaction of Radiation with matter

The electromagnetic and particulate radiation emitted from the atomic nuclei in different nuclear processes is called nuclear radiation, due to its origin. Typically radiation is made up of heavy charged particles (protons, alpha particles, heavy ions, mesons), electrons and positrons, X-rays and gamma rays, and neu-

trons. Nuclear radiation is considered to be ionizing. X-rays are, like gamma radiation, photons, and depending on the material they interact with and their energy, can or not be ionizing. X-rays are not nuclear radiation since they do not originate from atomic nuclei, but from the electronic cloud, unlike gamma rays.

The principle for the energy loss of heavy charged nuclear particles is ionization, as well as excitation of the electrons of the absorber atoms. According to classical mechanics the maximum energy  $E_{max}$  that an electron of mass  $m_0$  can acquire in a collision with a particle of mass  $M$  and energy  $E$  is given by

$$E_{max} = \frac{4m_0ME}{(m_0 + M)^2} \simeq \frac{4Em_0}{M}, \quad (1.1)$$

For energies up to 10 MeV, electrons lose their energy mainly by excitation and ionization of the electrons of the medium as in the case of heavy charged particles. For higher energy electrons the loss of energy as bremsstrahlung becomes increasingly important and the intensity of this varies as  $Z^2$  where  $Z$  is the atomic number of the medium [3]. During absorption due to ionization, owing to the lower mass of the electron compared to that of a heavy charged particle, a much greater fraction of the particle energy is transferred to the absorber electron in each collision, resulting in a path with considerable num-



ber of deflections. The rate of energy loss and the density of ionization are correspondingly less since an electron travels with much higher velocity than a heavy charged particle of the same energy thereby spending less time in the vicinity of the absorber atoms [5].

As commented above, gamma rays and X-rays are two forms of electromagnetic radiation differing only in their origins. Gamma rays are produced in nuclear reactions and represent a means to de-excite a nucleus, whereas X-rays are caused by the excitation or removal of orbital electrons or by the deceleration of electrons. We know that it is possible to associate a value of energy,  $E$ , to the wavelength,  $\lambda$ , that characterizes certain radiation.

$$E = h\nu = \frac{hc}{\lambda}, \quad (1.2)$$

where  $h$  = Plank's constant =  $6.63 \times 10^{-34}$  J s<sup>-1</sup>,  $c$  = velocity of light =  $2.9987 \times 10^8$  m s<sup>-1</sup>, and  $\nu$  = frequency.

The energy released upon the return of the orbital electrons to the ground state appears as X-ray photons also known as fluorescent radiation, or *characteristic X-rays*. Here it is convenient to note that there are fluorescent processes and phosphorescent processes, basically distinguished by their mechanism of occurrence, which has direct incidence in their lifetime. Fluorescence is primarily

concerned with electronic and vibrational states. Generally, we have a ground electronic state (a low energy state) of interest, and an excited electronic state of higher energy. Within each of these electronic states are various vibrational states. In fluorescence spectroscopy, the sample is first excited, by absorbing a photon, from its ground electronic state to one of the various vibrational states in the excited electronic state. Collisions with other molecules cause the excited molecule to lose vibrational energy until it reaches the lowest vibrational state of the excited electronic state as shown in Fig.1.1. The molecule then drops down to one of the various vibrational levels of the ground electronic state again, emitting a photon in the process. As molecules may drop down into any of several vibrational levels in the ground state, the emitted photons will have different energies [6]. In Fig.1.2, we can observe the transitions from ground state to different excited electronic states depending on the initial energy.

Unlike fluorescence, phosphorescence is a process in which energy absorbed by a substance is released relatively slowly in the form of light. In phosphorescence, the absorbed photon energy undergoes an inter system crossing into an energy state of higher spin multiplicity, usually a triplet state. As a result, the energy can become trapped in the triplet state with only classically “forbidden” transitions available to return to the lower energy state. These transitions, al-

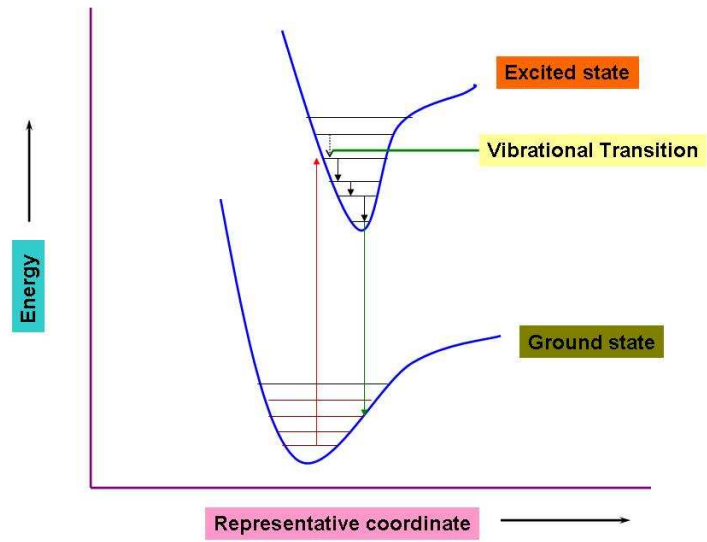


Figure 1.1: The origin of fluorescence

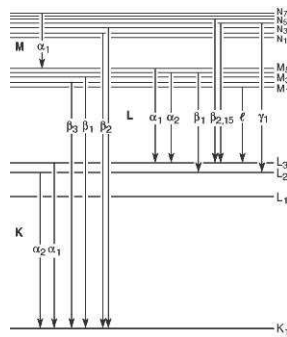


Figure 1.2: Transitions that give rise to various emission lines

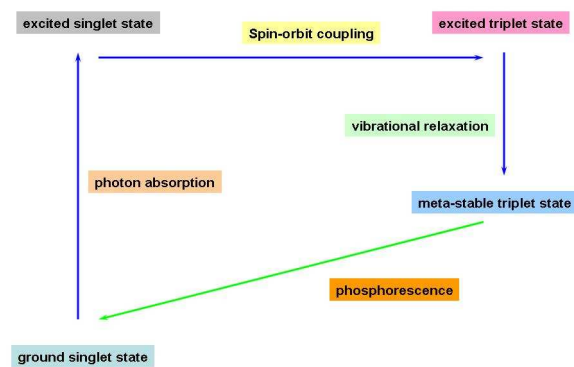


Figure 1.3: Phosphorescence

though “forbidden”, will still occur in quantum mechanics but are kinetically unfavored and thus progress at significantly slower time scales. If the molecules of the substance can get from the ground state to a metastable state, and if the metastable state can slowly decay back to the ground state via photon emission, then we have phosphorescence. Typically, the metastable state is a triplet state, and the ground state is a singlet state. Ground state (total spin quantum number  $S=0$ ) molecules absorb photons and go to excited singlet states (see Fig.1.3). During the collisions, the molecule can undergo transitions to a lower vibrational level that might have the same energy as one of the levels in the triplet ( $S=1$ ) excited state and then there is a certain probability for a shift to the triplet state to occur. But generally, most of them immediately hop

right back to the ground state, emitting a photon, and only a few non-radiative processes take to a less energetic triplet state. Once these molecules get to the lowest triplet state, they are stuck there, at least for a while. Some low probability process accomplishes the triplet-singlet conversion, and the molecules slowly leak out radiation [6]. In the present study, the discussion is oriented towards the fluorescence studies using the gamma and x-rays and no more will be discussed about the phosphorescence.

Gamma rays and X-rays interact with matter by one of three types of process, namely the photoelectric effect, Compton scattering and pair production. More will be discussed later in this chapter.

## 1.2 Mechanisms of Gamma Ray Interactions

As indicated in Section 1.1, the interaction of gamma rays with matter is primarily through three mechanisms. The illustrations of these mechanisms are shown in Fig.1.4.

In the photoelectric effect a photon of energy  $h\nu$  interacts with the atom as a whole [8]. Its energy is transferred to an electron, normally one in the innermost shell. The electron is ejected with a kinetic energy given by,

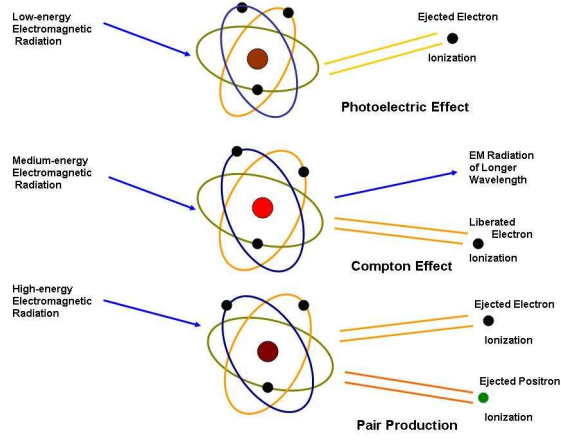


Figure 1.4: Mechanisms of gamma ray interactions [5].

$$E_{kin} = h\nu - E_b, \quad (1.3)$$

where  $E_b$  is the binding energy of the orbital electron. The original gamma ray or X-ray disappears in this process and since the atom is left with a vacancy in an atomic shell, it will be immediately filled, in about few ns, by an outer electron and an X-ray will be emitted. Compton scattering is considered to be an inelastic collision between a photon and an atomic electron, in which the electron binding energy is very small compared with the photon energy. The energy is shared between the scattered photon and the recoiling electron. Part of the energy of the incident photon is carried away by the electron and the rest appears in the form of a photon of higher wavelength or equivalently,

lower energy. If the incident photon has a frequency  $\nu$  associated with it, the scattered photon has the lower frequency (higher wavelength)  $\nu'$ , where we can see that the loss in photon energy is equal to the gain in electron energy as in Eq.1.5. Energy and momentum are conserved in this process and this is the chief process through which X-rays lose energy when they pass through matter [6]. The Compton scattering phenomenon can be observed in Fig.1.4. Application of the laws of conservation of momentum to the collision of a photon with a free electron leads to the following expression,

$$h\nu' = \frac{h\nu}{1 + (1 - \cos \theta)h\nu/mc^2}, \quad (1.4)$$

where  $h\nu'$  is the energy of the scattered photon and  $\theta$  is the angle between its direction and that of the incident photon. The kinetic energy  $E_{kin}$  of the recoil electron is

$$E_{kin} = h\nu - h\nu' = h\nu \left[ \frac{(1 - \cos \theta)h\nu/mc^2}{1 + (1 - \cos \theta)h\nu/mc^2} \right], \quad (1.5)$$

Recoil electrons may have any energy between zero and a maximum corresponding to a minimum value of  $h\nu'$  which occurs for a backscattered photon,  $\theta = 180^\circ$ .

$$(E_{kin})_{max} = \frac{2(h\nu)^2}{(mc^2 + 2h\nu)}, \quad (1.6)$$

In the pair-production process, the gamma ray disappears, and a positron and an electron are produced. For this to happen the gamma ray energy must be larger than the total rest-mass energy of the pair and this process should occur within the Coulomb field of a nucleus. Any excess energy appears as kinetic energy,  $E_{kin}$ , of the electron positron pair, and a very small recoil energy is imparted to the nucleus [10].

$$E_{kin} = h\nu - 2mc^2 = h\nu - 1.02 \text{ Mev}, \quad (1.7)$$

### 1.3 X-Ray Physics

Earlier we have already discussed some aspects of the interaction of radiation and matter. In this section we will continue the discussion but with a concentration on X-ray radiation alone. Actually we will look at fundamental expressions relating the emitted intensity to the concentration of the element in the specimen whose characteristic X-ray spectrum is measured. Most topics, e.g. electronic transitions, absorption and scatter of X-rays etc., are covered only to the extent that they relate, closely, to conventional X-ray fluorescence



analysis.

### 1.3.1 Continuous and Characteristic Radiation

When a high-energy electron beam is incident upon a sample, two kinds of interactions are observed, one being an emission of a broad wavelength band of radiation called *bremssstrahlung*, also called continuum or white radiation, and the other one called *characteristic radiation*. The latter one, corresponds to radiation produced when the impinging electrons are decelerated during their interaction with matter. An intensity vs. wavelength representation is typified by a minimum wavelength  $\lambda_{min}$ , which is inversely proportional to the maximum accelerating potential  $V$  of the electrons. An increase in the accelerating potential causes the intensity distribution of the continuum to shift towards shorter wavelengths. Actually the kinetic energy of the atomic electron can be expressed as indicated in Eq.1.3.

### 1.3.2 X-ray Spectra

During the process of photoelectric effect, energy stability conditions in the atom will require that another electron from a higher shell would move to occupy the previously formed vacancy, and while doing so the electron gives

out radiation in the form of an x-ray photon that corresponds to the energy difference of the two positions. There is an expression, devised by Moseley [8] that relates the energy of the participating shells,  $E$ , and the atomic number,  $Z$ ,

$$E = K(Z - \sigma)^2, \quad (1.8)$$

where,  $K$  is a constant that takes on different values for each spectral series, and  $\sigma$  is the shielding constant of value less than unity.

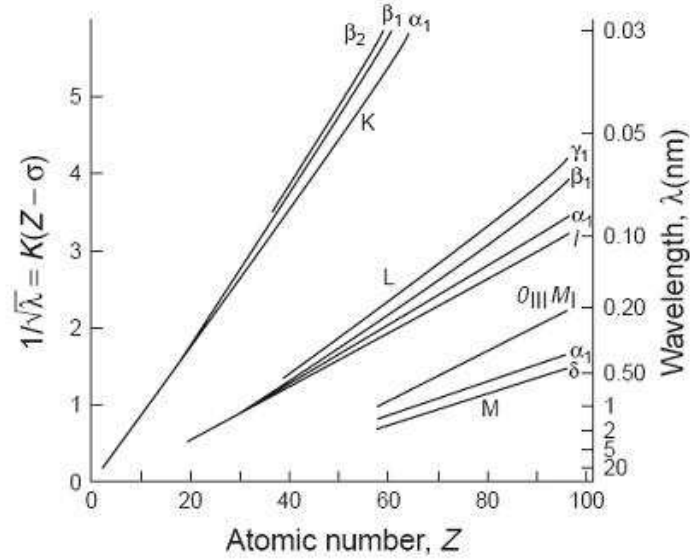


Figure 1.5: Moseley diagrams for the K, L and M series [8]

It should be noted that not all vacancies result in the production of X-ray

photons, since there is a competing phenomenon known as the Auger process, a radiationless transition, where the ejection of another electron occurs, resulting in double ionization of the atom. Thus the fluorescence yield can be expressed in the next manner:

$$\omega = \frac{Z^4}{A + Z^4}, \quad (1.9)$$

where  $A$  = constant that depends on the atomic shell involved, given an atom of atomic number  $Z$ . The Auger yield is given as  $1-\omega$ . A plot of both yields would show that for low  $Z$  elements, the Auger process will be predominant [7].

## 1.4 Attenuation of Gamma Radiation

The number of gamma or X-ray photons diminishes during interaction with matter, either by scattering or absorption. Hence the intensity variation as a function of absorber thickness is given by

$$\frac{I_{trans}}{I_0} = e^{-\mu t}, \quad (1.10)$$

where  $I/I_0$  is the fraction of photons remaining in the beam after passage through a material of thickness  $t$ . This equation relates the intensity of gamma-rays at a specified energy after attenuation,  $I$ , to that without attenuation at

the same energy,  $I_0$ .

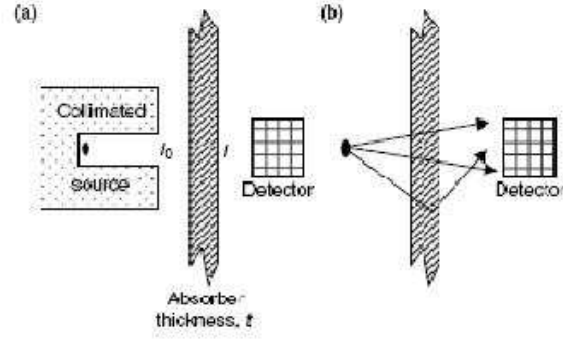


Figure 1.6: (a) Attenuation of a beam of gamma-rays from a collimated source with intensity  $I_0$ ; note that after the attenuator the intensity has a value of  $I$ . (b) A lack of collimation of the incident beam implies a more complicated irradiation geometry.

The quantity  $\mu$  is known as the total linear attenuation coefficient. Strictly  $\mu$  is expressed as:

$$\mu = \tau + \sigma + \kappa, \quad (1.11)$$

where  $\tau$ ,  $\sigma$ ,  $\kappa$  represent the partial coefficients due to the photoelectric effect, Compton effect, and pair production, respectively.

The relationship, Eq.1.10, is only valid under “good geometry” conditions, Fig.1.6.(a). Under the conditions like those pictured in Fig. 1.6.(b)., the equa-

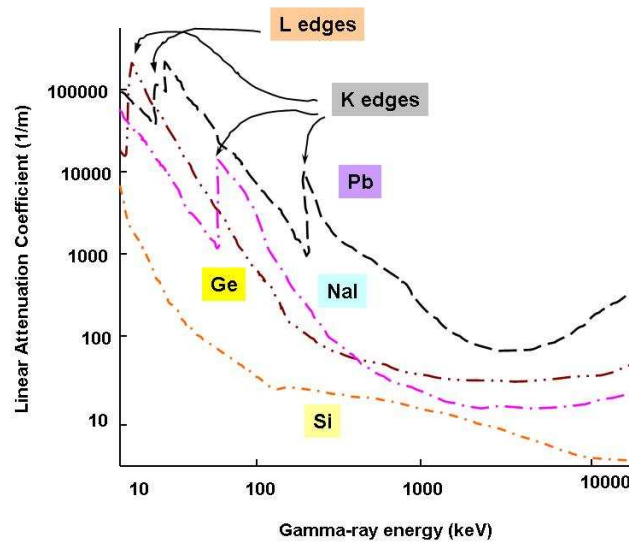


Figure 1.7: Attenuation coefficient of materials as a function of gamma energy [4].

tion fails mostly because of scattering from the absorber. Fig.1.7 shows the behavior as a function of energy, of some attenuation coefficients. Some features to highlight in Fig.1.7 are the sharp drops at certain values of energy.

Fig.1.7 highlights another interesting tendency, that is, the dependence of the attenuation coefficient on the atomic number,  $Z$  [10]. Germanium, for instance, is a better detector material than silicon. Fig.1.8 shows the attenuation and absorption coefficients of Ge.

It may important at this point to define the terms attenuation coefficient

and absorption coefficient. An attenuation coefficient is a measure of the reduction of the number of photons that are scattered away from the detector by a material placed before the detector itself can be reached by the radiation.

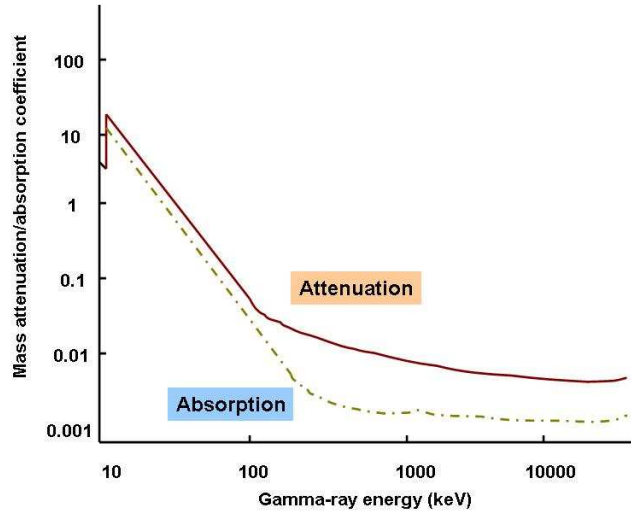


Figure 1.8: Comparison of Attenuation coefficient and absorption coefficients of Ge [5]

The absorption coefficient is related to the amount of energy retained by the absorber material as the radiation passes through it, that is, transferring energy to the electrons in the material. Energy transferred to the electrons represents the energy absorbed by the detector, if so the absorbing material is used and is, in turn, related to the output from the detector in that case.

## Chapter 2

# Semiconductor Detectors for Spectroscopy

In this chapter it is attempted to discuss some generalities of semiconductors in the context of radiation detection. Earlier we have discussed how gamma radiation interacts with matter through various mechanisms, by which energy has been transferred to electrons and, in the case of pair production, positrons. The process by which the radiation is absorbed involves the production of one or more high-energy secondary electrons resulting from the primary radiation, so that a cascade process continues until no further ionization is possible. At this point, it should be clear that the detection process is closely dependent

on the number of ion pairs created, likewise linked to the amount of energy deposited.

## **2.1 Semiconductors and EM-Radiation Detection**

### **2.1.1 The band structure of solids**

When we consider a free atom, the electrons are disposed in precisely determined energy levels. Combining a collection of atoms together into a solid structure broadens those energy levels into energy bands, each of which can contain a fixed number of electrons. Between these bands there will arise energy regions that are forbidden to electrons. Energy-wise, the uppermost region, constitutes a band where the occupying electrons are responsible for chemical reactions, this is known as the valence band. Certain processes may require electrons to migrate about within the solid, and in order for that to happen, the electron must be able to move out of its initial energy state into another. An externally applied electric field can additionally contribute to motion of an electron about the solid, an aspect that will be of relevance in radiation detection.



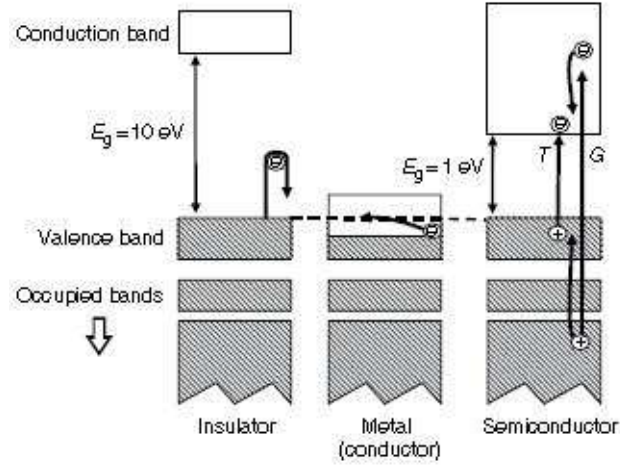


Figure 2.1: Schematics of the electronic band structures in insulators, metals and semiconductors [11].

Materials can be basically classified in the next three categories, Fig. 2.1: insulators, conductors and semiconductors. In an insulator, the valence band is full and the next available energy states are in a higher band, called the conduction band, separated by the aforementioned forbidden region. Migration of the electron through the material can only be accomplished if the electron jumps across the the band gap,  $E_g$ , into the conduction band. Typically  $E_g \approx 10$  eV for an insulator, which is grater than the energy produced by thermal excitation.

In a metal, the valence bands are not full and in effect the conduction band is basically continuous with the valence band. Thermal excitation ensures that

the conduction band is always populated to some extent and the imposition of an electric field, however small, will cause a current to flow, which allows the material to exhibit some degree of conductivity [1]. The band structure of semiconductors is not dissimilar to that of insulators. The valence bands are full but the band gap is much smaller, of the order of 1 eV, i.e., comparable to thermal excitation [1].

The Boltzmann distribution equation, Eq. 2.1, represents the probability that an electron will be promoted to the conduction band under influence of the temperature,  $T$ :

$$p(T) \approx T^{-3/2} \exp(-E_g/2kT), \quad (2.1)$$

where  $k$  = Boltzmann's constant.

### **2.1.2 Creation of charge carriers by gamma radiation**

The interaction of a gamma photon with the semiconductor material will produce primary electrons with energies well above thermal energies. Such electrons can rise from deep occupied bands into energy levels well above the conduction band's base. These holes and electrons created will tend to redistribute themselves within the available energy bands until the holes lie at the top of

the valence band and the electrons at the base of the conduction band, Fig. 2.1. The number of electron-hole pairs produced,  $n$ , will be related directly to the gamma-ray energy absorbed,  $E_{abs}$ :

$$n = E_{abs}/\epsilon, \quad (2.2)$$

where  $\epsilon$  is the average energy needed to create an electron-hole pair [5].

Looking in perspective at the previous sections, it can be said that the ideal semiconductor detector material will:

- have as large an absorption coefficient as possible, thus a high atomic number,
- provide as many electron-hole pairs as possible per unit energy, i.e. small value  $\epsilon$ ,
- allow good electron and hole mobility, and
- be available in high purity single crystals.

The above features are fulfilled by some materials; examples are shown in Table.2.1. The most commonly used materials are silicon and germanium, backed by long experience from the electronics industry. Germanium is particularly much used to detect high energy gammas [11].

Table 2.1: Parameters of some materials suitable for gamma-ray detectors. For  $\epsilon$  the values indicated are given at 77K for Ge and 300K otherwise [11].

Material	Atomic number	Band gap[eV]	$\epsilon$ [eV]	Density [g cm <sup>-3</sup> ]
Si	14	1.106	3.62	2.33
Ge	32	0.67	2.96	5.32
CdTe	48,52	1.47	4.43	6.06
CdZnTe	48,30,52	1.57	4.64	5.78

Cadmium telluride (CdTe) and cadmium zinc telluride (CZT) are good detector materials that have found their way into commercial production. Nevertheless, it should be noted that the charge carrier mobilities in these materials are considerably lower than those for Ge. An additional caveat is the hole susceptibility for trapping which imposes severe charge collection problems on the detectors that limits their physical size.

The performance of CdTe and CZT detectors can be enhanced by novel electronic means, which compensate for the poor charge collection but yet, do not pair them with the features of Ge.

## 2.2 Operation of a semiconductor detector

When radiation falls on a detector, as discussed previously, electron-hole pairs are produced. Subsequent charge collection by suitable electrodes, yields a signal with a height proportional to the energy expended by the radiation in the material. The number of electrons produced by the radiation should be much larger than the number of electrons already in the conduction band, which requires a small enough steady state current. Current thus produced is converted to a voltage pulse, by a capacitor and resistor, i.e. an RC circuit, such that one digital voltage pulse is produced for each entering photon, Fig. 2.2.

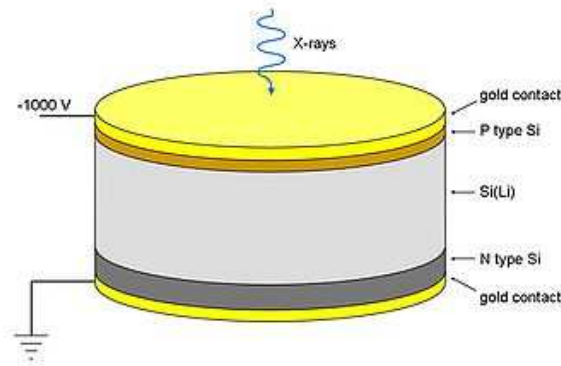


Figure 2.2: Basic structure of a semiconductor counter, in this case corresponding to a silicon lithium-drifted crystal, Si(Li) [28].

In addition to being sensitive to the appropriate photon energies, i.e. a

given range of wavelengths or energies, there are two other important properties that an ideal detector should possess: proportionality and linearity [8]. Proportionality is needed where the technique of pulse height selection is to be used. Pulse height selection is a means of electronically rejecting pulses of voltage levels other than those corresponding to the characteristic line being measured. Photons enter the detector at a certain rate, and if the output pulses are produced at this same rate, the detector is said to be linear. Linearity is important when photon intensity is to be measured.

## 2.3 Charge collection in Detectors

In this section we briefly discuss some additional details that will help to understand better how charge collection and charge mobility of carriers take place.

### 2.3.1 Charge collection time

To start with, let us consider a parallel plate type of detector, Fig. 2.2. An electron-hole pair, created at a distance  $x$  from the positive electrode,  $n+$ , without any external persuasion, will move within the lattice under the influence of thermal excitation. Next, application of an electric field,  $E$ , created by a bias voltage,  $V_b$ , will cause an additional drift motion parallel to the direction of the

field. Electrons will migrate to the positive collector and holes to the negative one, Fig. 2.3.

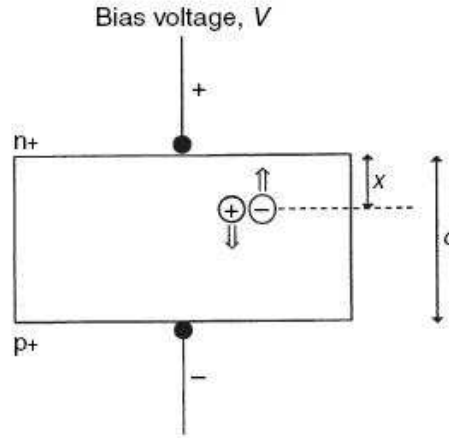


Figure 2.3: Charge carrier motion in a semiconductor detector

It is clear that the time taken for each charge carrier to reach its destination, the charge collection time, will depend upon the distance it must travel and the speed at which it travels. For each entity we can define a *mobility*,  $\mu$ , equal to the ratio  $\nu/E$ , where  $\nu$  is the *drift velocity* of the electron or hole and  $E$  the electric field strength.

At low field the mobility is almost constant, but at high field the drift velocity does not increase in proportion to the field magnitude and eventually reaches a saturation velocity [17]. If we provide a detector with a great enough bias voltage to ensure that the field strength is sufficient to give all charge

carriers their saturation velocity throughout, we can easily calculate the charge collection time, considering the geometry in Fig.2.2:

- electron collection time,  $t_e = x/\nu_e$ ,
- hole collection time,  $t_h = (d - x)/\nu_h$ ,

where  $\nu_e$  and  $\nu_h$  are the saturation velocities of electrons and holes, respectively, and  $x$  and  $d$  are defined in Fig.2.3. If we look now at the position at which the electron-hole pair is created relative to the positive and negative collectors of the detector, then we can appreciate that the electrons and holes will arrive at different times. The electron from an event close to the positive electrode will be collected well before the hole has time to travel to the negative electrode. This, in turn, means that the way in which the output pulse from the detector rises will depend upon the position at which the charge carriers are produced.

### 2.3.2 Trapping of charge carriers

In a semiconductor detector it is often important that the total charge produced by the primary particle be collected at the electrodes and contribute fully to the signal. This condition is a requirement in high-resolution spectrometry. One important consequence of insufficient charge collection is the dependence



of pulse size on the applied voltage. Another consequence is a degradation of the resolution of the detector. In addition there are other deleterious effects if the charges are not swept out of the detector. One such effect is the polarization phenomenon, in which the charge accumulated in the interior of the detector sets up an internal field opposed to that produced by the external applied collecting voltage [2].

We have assumed so far that the electrons and holes are free to migrate, unhindered, to the collector contacts. In any detector crystal there is likely to be a small population of traps. These might be a consequence of crystal imperfections, interstitial impurities, or radiation damage. If a charge carrier migrates to one of these traps it may be held until thermal excitation releases it again. The average time that a carrier might spend in such a trap depends upon the depth of the trap in terms of energy [3].

The efficiency of charge collection  $\eta$  may be denoted by

$$\eta = \frac{q}{Ne} \tag{2.3}$$

where  $q$  is the charge on the collecting electrode,  $N$  is the number of electron-hole pairs released, and  $e$  is the charge of the electron.

The trapping phenomenon applies to both holes and electrons. The trapping

centers do not necessarily destroy the charge carrier, but rather may immobilize it and thereby interrupt its contribution to the current. The loss of a charge carrier through recombination takes place primarily through a two-step process brought about by centers located within the forbidden energy gaps of the solid [5] but this topic will not be discussed any deeper.

# Chapter 3

## Experimental development

In this chapter, we discuss about the materials used for elemental analysis using energy-dispersive XRF. It will be discussed the operational characteristics of the x-ray source (COOL-X), Si(Li) Pin detector and CdTe detector used in the analysis here presented; all manufactured by Amptek, Inc. In context with the material covered in this thesis, specific details about the calibration techniques and the detectors will be explained.

### 3.1 X-ray Generator

The miniature X-ray generator, popularly known as COOL-X (Amptek, Bedford, MA, USA), uses  $\text{LiTaO}_3$  [41], a pyroelectric crystal [13] that produces

X-rays from Cu and Ta; its operation will be discussed later.

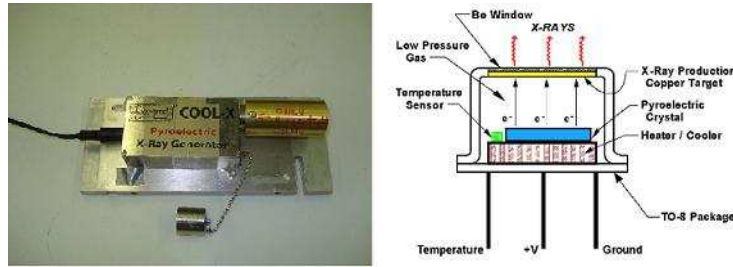


Figure 3.1: Production of X-rays is achieved through the COOL-X Generator.

To the left we have the physical COOL-X generator, and to the right a schematic of the x-ray generating system, contained in the nozzle of the actual physical device [13].

### 3.1.1 Theory of operation

The COOL-X, Fig. 3.1, generates x-rays via a polarization phenomenon. By changing the temperature of a pyroelectric crystal in the presence of a low pressure gas, polarization of the crystal occurs. As the temperature increases, an electric field develops across the crystal so that electrons are accelerated toward the Cu plate, and during the cooling period of the temperature cycle, electrons strike the crystal, which contains among other elements, Ta. Given the former, Cu as well as Ta characteristic x-rays are produced following an

alternative cycle. Fig. 3.2 shows the typical spectrum of the generator with the dominant 8 keV peak superimposed on the bremsstrahlung.

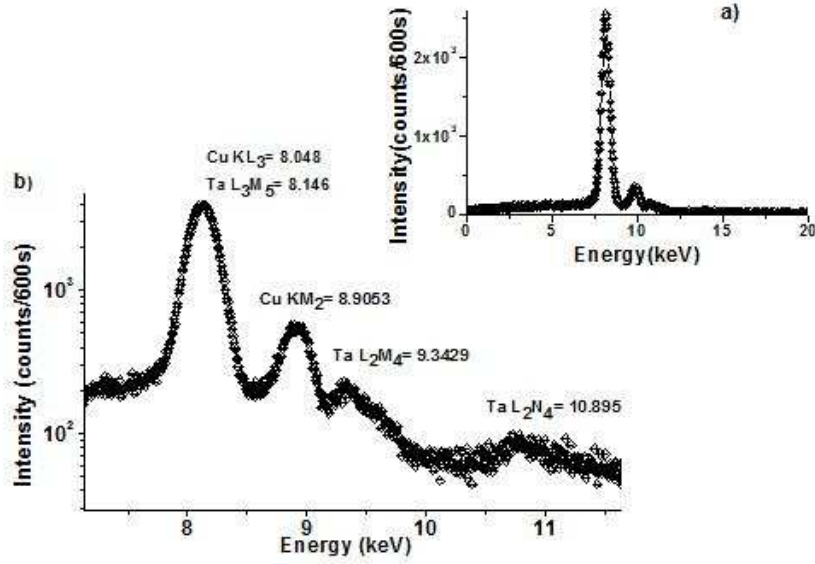


Figure 3.2: The spectrum from the COOL-X pyrolithic generator is observed in (a) linear and in (b) log scale.

## 3.2 Samples

The metallic alloys considered for experimental analysis in this thesis are Nickel foil (99.95% purity, 0.009 mm thick produced by Goodfellow), aluminium (Al) and lead (Pb) scrap plates. The Standard Reference Materials (SRM) were



Figure 3.3: Metallic alloys and Standard Reference Materials (SRM) used as samples in the XRF measurements in this thesis. The specific SRMs used are: C2417, 1240cAl, and 1159EM. All SRMs were obtained from the National Institute of Standards and Technology, NIST.

purchased from the National Institute of Standdards and Technology (NIST). In this particular analysis three SRMs were used: 1240c Aluminium Alloy 3004, C2417 Lead-Base Alloy and 1159 Electronic and Magnetic Alloy, Fig. 3.3.

### 3.3 General methodology

In the present work x-rays from the COOL-X generator were calibrated using the PyMca software [30]. The methodology through which the PyMca cali-

brates the spectrum obtained is described in Section 3.6 and in Appendix B. Power consumption during x-ray production is typically less than 300 mW. The x-ray output flux varied during the first 2 to 5 minutes of the thermal cycle yielding a maximum flux of about  $10^8$  photons/s, equivalent to a 2 mCi source;  $1 \text{ Ci} = 3.7 \times 10^{10} \text{ decay s}^{-1}$ . During warm-up the device produces Ta-L lines, and during cool-down the Cu-K lines are excited. X-rays are collected using either CdTe or Si(Li) detector. The signal from the detector was routed into a personal computer through a multichannel analyzer MCA8000A, produced by Amptek, and each spectrum was analyzed using the PyMca software. Energy and peak width calibrations are performed on the obtained spectrum.

### **3.4 Si(Li) Pin X-ray Detector (XR-100CR)**

The XR-100CR has a thermoelectrically cooled Si(Li) Pin photodiode as an x-ray detector. The input FET and the feedback circuit are mounted on the two-stage cooler that helps maintain the temperature to approximately  $-55^\circ\text{C}$ . This device has a very thin vacuum tight Beryllium window to enable soft x-ray detection. The PX2CR contains most of the electronics required by the XR-100CR and it also sends a signal to the MCA. This Si(Li) detector consists of a small cylinder (about 1 cm diameter and 3 mm thick) of p-type silicon

that has been compensated by lithium to increase its electrical resistivity which enables the possibility of applying a large bias voltage and thus producing thick depletion regions, that is a wide *i* or intrinsic region, where detection takes place. A Schottky barrier contact, i.e a metal-semiconductor contact, on the front of the silicon disk produces a p-i-n type diode; positive-intrinsic-negative. In order to inhibit the mobility of the lithium ions and to reduce the electronic noise, the diode and its preamplifier are typically cooled to the temperature of liquid nitrogen, about 77K, although nowadays the perfection of semiconductor detectors allows the use of thermoelectric cooling, as indicated above, without the constant need of maintaining the detector in contact with liquid N<sub>2</sub>. The particular detector used in the present work, XR-100CR Si(Li) pin detector, has specifications of 13 mm<sup>2</sup> effective detection area, 300  $\mu$ m thickness, 1-mil (25 $\mu$ m) thick Be window, and an energy resolution of 219 eV at 5.9 keV x-rays.

### 3.4.1 Theory of operation

Incident x-rays interact with silicon atoms to produce a specific number of electron hole pairs. One electron/hole pair on an average is created for every 3.62 eV of energy lost in the silicon. This loss is overcome by either the Photoelectric effect or Compton scattering depending on the incoming radiation energy.





Figure 3.4: To the left we can observe the XR-100CR Si-Pin X-ray detector, and to the right a schematic of the internal structure of the detector [13].

The efficiency of the detector to create an electron/hole pair increases with the thickness of the silicon. A range of 100-200 volt bias voltage is applied across the Si depending on the detector thickness in order to enable electron/hole collection. The primary advantage of the higher voltage is that it decreases the capacitance and increases the transconductance, which reduces the electronic noise. Electronic noise is additionally diminished by cooling.

The charge produced is swept from the diode by the bias voltage to a charge sensitive pre-amplifier. The charge loop integrates the charge on a capacitor to produce an output pulse. The pre-amplifier collects this charge on a feedback capacitor to produce a voltage pulse proportional to the original x-ray photon energy. Therefore when a range of photon energies are incident upon the Si(Li)

detector, an equivalent range of voltage pulses are produced as the output. Then the multichannel analyzer is used to sort the arriving voltage pulses at its input in the same manner, thereby resulting in a histogram representation of the x-ray energy spectrum. The feedback method is used for resetting of the charge sensitive amplifier, which is performed through the high voltage connection to the detector by injecting a charge pulse through the detector capacitance to the input FET, field-effect transistor. This method is used to improve the energy resolution of the detector system.

### **3.5 CdTe X-ray and Gamma Ray Detector**

XR-100T CdTe is a high performance x-ray and gamma ray detector, preamplifier, and cooler system using a  $7\text{ mm}^2$  Cadmium Telluride (CdTe) diode detector mounted on a two-stage thermoelectric cooler. Also on the cooler there are allocated the input FET feedback components to the charge sensitive preamplifier. The internal components are kept at approximately  $-30\text{ }^{\circ}\text{C}$  and can be monitored by an internal temperature sensor [13]. The PX2T contains most of the electronics required by the XR-100T CdTe and it also sends a signal to the MCA. The hermetic package enclosing the detector has a light tight, vacuum tight, 1 mil ( $25\mu\text{m}$ ) Beryllium window. The technical specifications

are provided in Appendix A.3.



Figure 3.5: XR-100T CdTe X-ray detector.

### 3.5.1 Theory of operation

X-rays and gamma rays interact with CdTe atoms to create an average of one electron-hole pair for every 4.43 eV of energy lost in the CdTe. The probability or efficiency of the detector to capture the incoming radiation and create electron-hole pairs increases with the thickness of CdTe. In order to facilitate the electron-hole collection process in the CdTe detector, a +500 V potential is applied. Since the detector in the XR-100T CdTe is cooled, the leakage current is reduced considerably, thus permitting application of a high bias voltage. Addition of the FET transistor to the charge sensitive preamplifier results in increasing the transconductance, which in turn reduce furthermore the electronic

noise of the system [13].

### 3.5.2 Charge trapping in XR-100T CdTe

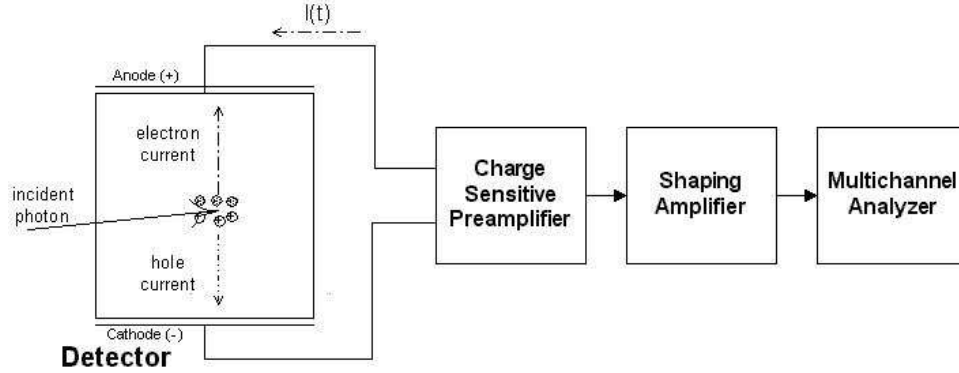


Figure 3.6: Schematic diagram of the detector and electronics.

Considering the charge transport and signal generation process sketched in Fig. 3.6, we can see that at the electric field strengths usually found in a radiation detector, the drift velocity  $v$  of the carriers is proportional to the electric field strength  $\varepsilon$ , where the constant of proportionality is defined as the mobility  $\mu$ ,  $v = \mu\varepsilon$ . The instantaneous current is  $I = qnv$ , where  $q$  is the charge on an electron,  $n$  is the number of carriers, and  $v$  is their mean velocity. Considering the case of a uniform, planar detector of thickness  $L$ , with a bias  $V$ , it is possible to obtain a constant and uniform electric field,  $\varepsilon = V/L$ .

## 3.6 Spectrometer Calibration

Spectrometer calibration allows the gamma- or X-ray spectrum to be interpreted in terms of energy, rather than channel number. Typically a spectrum is collected using a multichannel analyzer that yields spectrum information directly binned into a prescribed number of channels, each of them corresponding to some energy value.

There are mainly three calibration tasks required to characterize an energy spectrum :

- energy calibration,
- peak width calibration,
- efficiency calibration.

In practice, spectrometers are calibrated using well characterized gamma- or x-ray spectra.

### 3.6.1 Sources and Reference Data for Calibration

In the present work, calibration takes place using gamma sources with known probability of emission, half-life, and activity. The activity of the radioactive sources used is about 1 micro-Curie [ $\mu Ci$ ].

### 3.6.2 Energy Calibration

The main purpose of energy calibration is to derive a relationship between peak position, given as a channel number in the spectrum, and its corresponding energy.

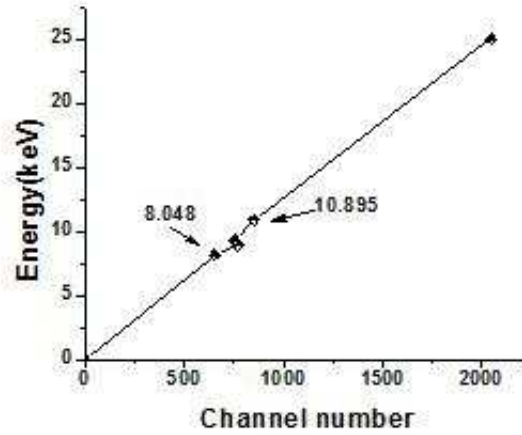


Figure 3.7: Energy Calibration of the pyroelectric X-ray source using two characteristic energy lines, Cu  $KL_3 = 8.048$  keV and Ta  $L_2N_4 = 10.895$  keV. As it will be discussed later on, the pyroelectric X-ray source contains a crystal made of  $LiTaO_3$  that gives rise to characteristic radiation.

As noted above, the calibration process requires a list of energy peaks that are to be identified in the spectrum and statistically treated through a linear correlation process in a manual way [24] in order to assign a energy-to-channel

relationship. Alternatively there are computer programs that allow for a linear regression calculation. The linear regression process entails identifying an energy intercept,  $I$  [keV], and a slope or gradient,  $G$  [keV/channel]:

$$E(keV) = I(keV) + G \times C(channels), \quad (3.1)$$

where  $C$  is the channel position. It should be clear that improper identification of the characteristic lines produces an error that propagates into the calibration, affecting any further measurements based on it, thus proper care has to be followed at this step.

### 3.6.3 Peak Width Calibration

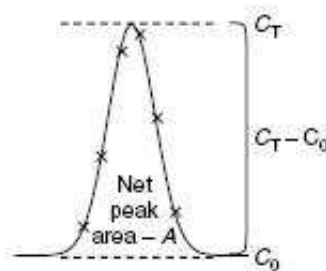


Figure 3.8: Estimating FWHM using the area/height ratio.

Quite often it is assumed that peaks have a Gaussian shape, but that need not be the case always, and proper adjustments are to be considered. The

experimental treatments of this work assume that peaks have a Gaussian shape in general. Bearing in mind Fig. 3.8, initially we estimate the peak height,  $C_T$  and then subtract the peak background,  $C_0$ , based upon the *average background level* above and below the peak.

$$FWHM = 0.939 \times A/(C_T - C_0), \quad (3.2)$$

where  $A$  is the area of the peak and the denominator is the full height of the peak corrected for underlying background. This formula can be derived very simply from the analytical expression for a Gaussian such as is given in Eq. 3.2, where  $FWHM$  = full width at half maximum. Unless the peak is centered on a channel, estimating the height needs either simple interpolation or a more elaborate calculation. For this reason, if the  $FWHM$  is measured to check the system resolution the amplifier gain must be adjusted very slightly so that the centroid of the appropriate peak is centered on a channel, as in Fig.3.9.

The channel contents in a Gaussian peak can be related by the equation:

$$C_i = C_0 + C_T \exp \left[ \frac{-(x - \bar{x})^2}{2\sigma^2} \right], \quad (3.3)$$

Substituting the data for the channels on both sides of the centroid,  $\bar{x}$ , Fig. 3.9 provides us with two equations which can be divided and rearranged to



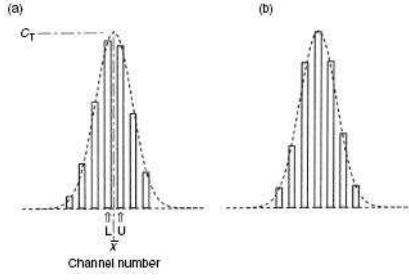


Figure 3.9: Maximum peak height located in two different situations: (a) between two channels and (b) centered about a particular channel.

derive:

$$C_T = \exp \left[ \frac{\ln(C_L - C_0) - F \ln(C_U - C_0)}{(1 - F)} \right], \quad (3.4)$$

where  $F = \left(\frac{L - \bar{x}}{U - \bar{x}}\right)^2$ ,  $C_L$  = channels to the left of the centroid, and  $C_U$  = channels to the right of the centroid [11].

### 3.6.4 Various methods for Efficiency Calibration

There are various ways to undertake energy efficiency calibration:

- calibration using standard radioactive samples,
- calibration using photoelectron and Auger lines induced by high-energy x-rays,
- calibration using elastically backscattered electrons.

In this particular study, we are using the standard radioactive sources to perform the efficiency calibration and no more of the other two methods are discussed any further.

### **3.6.5 Importance of Calibration in XRF**

In studies involving activation analysis, almost all measurements are made comparatively. The samples and standards irradiated together are measured under identical conditions and their spectrum areas are compared directly. The calculations implicitly takes into account efficiency, including all of the factors likely to cause error. In this study, a limited set of radionuclides are used and there is a great deal of merit in making measurements relative to a reference standard for each radioactive source rather than depending upon the interpolation of a calibration curve, as the later introduces extra uncertainties over and above those involved in producing a point on the curve. The key factors which make calibration a must for these techniques are:

- effect of source to detector distance,
- effect of source density on efficiency,
- efficiency loss due to random summing (pile up),

- true coincidence summing

Uncertainties caused by these factors are responsible for wrongly estimating the efficiency of a detector and thereby produces a risk of providing incorrect elemental concentration estimates.

### 3.6.6 Efficiency Calibration

In quantitative X-ray fluorescence calculations we will be interested in relating elemental content to the intensities of spectral lines, which the detector will collect with different ability, or efficiency, depending on their specific energy as well as other additional factors. It will then be necessary to have a precise figure for the detector efficiency in order to relate the number of pulses counted to the number of photons incident on the detector. Absolute efficiency is defined [11] as

$$\epsilon_{abs} = \frac{\textit{number of pulses recorded}}{\textit{number of photons emitted by source}}, \quad (3.5)$$

and is dependent not only on detector properties but also on the details of the counting geometry such as the distance from the source to the detector. The intrinsic efficiency is defined [37] as

$$\epsilon_{int} = \frac{\text{number of counts in the spectrum}}{\text{number of photons incident on detector}}, \quad (3.6)$$

and the solid angle subtended by the detector is no longer included as an implicit factor. The intrinsic efficiency of a detector depends on the detector material, the radiation energy, and the physical thickness of the detector in the direction of the incident radiation. To relate both absolute and intrinsic efficiencies we use the next expression:

$$\epsilon_{abs} = \epsilon_{int} \left( \frac{\Omega}{4\pi} \right), \quad (3.7)$$

where  $\Omega$  is the solid angle of the detector as seen from the actual source position. It is convenient to tabulate values of intrinsic rather than absolute efficiencies because the geometric dependence is much easier to deal with for the former. Counting efficiencies are also categorized by the nature of the event recorded. The total efficiency is used when the entire area under the spectrum is a measure of the number of all pulses that are recorded, regardless of amplitude [35]. Fig. 3.10 is given as an example to understand how the intrinsic efficiency varies in the Si(Li) detector as the energy increases.

The calculation of full-energy peak efficiency is straightforward; it is the ratio of the number of counts detected in a peak to the number emitted by the

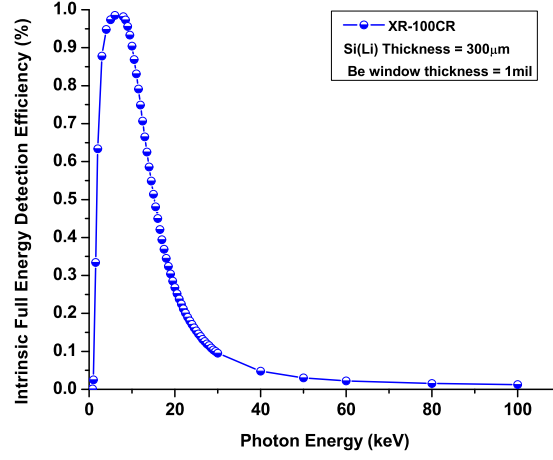


Figure 3.10: Linear plot of Intrinsic Full Energy Detection Efficiency vs Energy for a Si (Li) Pin Detector.

source [11]:

$$\epsilon = R/(S \cdot P_{\gamma}) \quad (3.8)$$

where  $R$  is the full-energy peak count rate in counts per second,  $S$  is the source strength in disintegrations per second (i.e. Becquerels, [Bq]) and  $P_{\gamma}$  is the probability of emission of the particular gamma-ray being measured. All information has to be adequately gathered from appropriate tables.

The Eq. 1.10 can be used here as each of the possible interaction process can be characterized by the probability of occurrence per unit path length of

the absorber. The number of primary photons interacting in a thickness  $t$  is:

$$I_{in} = I_0 [1 - e^{-\mu t}] \quad (3.9)$$

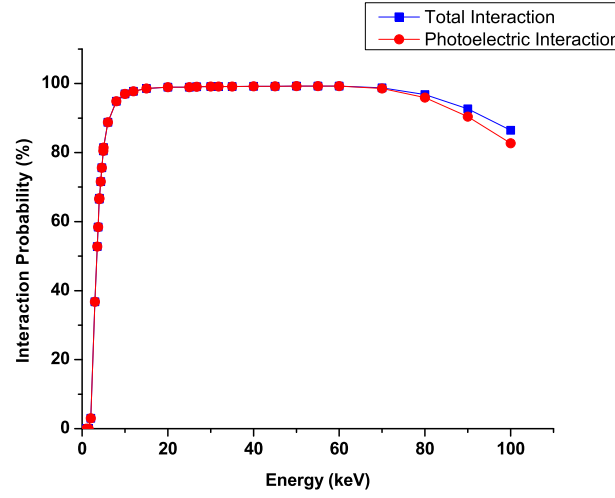


Figure 3.11: Linear plot of interaction probability vs energy for a CdTe detector [13].

Fig. 3.11 shows the linear plot of interaction probability over the lower energy range for a CdTe detector and the probabilities are calculated by using Eq. 3.10.

The probability of photon interaction somewhere in the detector thickness is the product of the probability of transmission through Be, the window material, and the probability of interaction in the material, CdTe:

$$P = (e^{-\mu_{Be}t_{Be}})(1 - e^{-\mu_{CdTe}t_{CdTe}}) \quad (3.10)$$

The relative photopeak efficiency of the detector can be obtained by using standard calibration sources in such a way that it covers the range of interest. The relative efficiency for a given source line is given by

$$\epsilon_i = \left( \frac{I_0 \cdot A_i}{A_0 \cdot I_i} \right) \quad (3.11)$$

where  $A_i$ ,  $I_i$  are the area and the relative intensity of the gamma line under consideration; they are to be consulted from published tables.  $A_0$  is the net photopeak area corresponding to the normalization gamma line, or most intense line, and  $I_0$  is the intensity of this line which is considered to be unity.

In this particular study the methodology involves the theoretical intrinsic efficiency-energy relationship [37] expressed by the equation :

$$\epsilon_i(E) = T(E) \times A(E) \times [1 - P_{esc}(E)], \quad (3.12)$$

where  $T(E)$  denotes the transmittance of the successive absorbing layers (Be window and Au contact),  $A(E)$  describes the absorption of photons in the sensitive volume of the detector,  $P_{esc}(E)$  is the probability of escape events,  $<2.5\%$ , considered negligible in the expected final uncertainty. The transmission and

absorption factors are expressed as below :

$$T(E) = \exp(-\Sigma\mu_l \times d_l), \quad (3.13)$$

and

$$A(E) = 1 - \exp(-\tau_a \times d_a) \quad (3.14)$$

where  $\mu_l$  is the total linear attenuation coefficient for x-rays with energy  $E$  and for material of layer  $l$ ,  $d_l$  is the layer thickness,  $\tau_a$  is the photoelectric absorption coefficient of the element  $a$ , either Si or CdTe, in the present case, and  $d_a$  is the detector thickness, composed of element  $a$ . Mass attenuation coefficients are taken from the certified NIST values.

And similarly the experimental intrinsic diode efficiency from observed peak areas and source activities is expressed as :

$$\epsilon_i(E) = \frac{N}{A \times t \times I \times T(E) \times \exp(-\mu_{air} \times d_{air}) \times (\Omega/4\pi)} \quad (3.15)$$

where  $N$ ,  $A$ ,  $t$ ,  $I$ ,  $T(E)$ ,  $\mu_{air}$  and  $\Omega$  are peak area, source activity, counting time, x-ray emission intensity, transmission factor, mass absorption coefficient of air and solid angle of detection, respectively. The solid angle of detection is calculated using a known expression [29] and obtained as  $2.460.06 \times 10^{-4}$ .



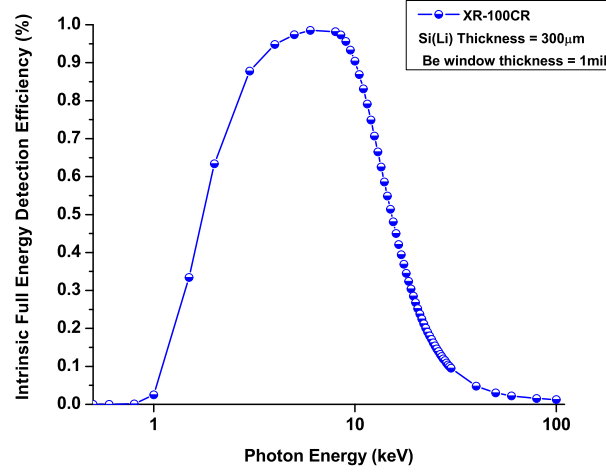


Figure 3.12: Plot between intrinsic efficiency and photon energy, in log scale, for a XR-100CR detector provided by [13].

Calibration of the Si(Li) Pin and CdTe detectors are performed using standard radioactive sources such as  $^{55}\text{Fe}$ ,  $^{241}\text{Am}$ ,  $^{137}\text{Cs}$  and  $^{133}\text{Ba}$ . The intensity probabilities of the radioactive sources are taken from X-ray and Gamma-Ray Standards for Detector Calibration, published by the International Atomic Energy Agency (IAEA). Table. 3.1 provides the values for the activity, energy, intensities which are required in order to calculate the theoretical and experimental efficiencies.

In order to find the theoretical intrinsic efficiency-energy relationship as in Eq. 3.12, apart from the attenuation data tables, the parameters from the

Table 3.1: Characteristics of radioactive sources used for calibration.

Radionuclide	Activity	Emission Type	Energy (keV)	Intensity (%)
$^{55}\text{Fe}$	(100 $\mu\text{Ci}$ )	X (Mn $K\alpha$ )	5.8988	16.56
T = 2.7 yrs.	A = $1.3703 \times 10^6$ Bq	X (Mn $K\beta$ )	6.49	3.4
		X (Np L1)	11.89	0.848
		X (Np L $\alpha$ )	13.9	13.03
$^{241}\text{Am}$	(0.9 $\mu\text{Ci}$ )	X (Np L $\beta$ )	17.81	18.86
T = 432 yrs.	A = $3.3 \times 10^4$ Bq	X (Np L $\gamma$ )	20.82	4.81
		$\gamma$	26.3446	2.4
		$\gamma$	59.5409	35.78
$^{137}\text{Cs}$	(5 $\mu\text{Ci}$ )	X (Ba $K\alpha$ )	32.1939	3.59
T = 30.2 yrs.	A = $18.5 \times 10^4$ Bq	X (Ba $K\beta$ )	36.67	1.055
		X (Cs $K\alpha$ )	30.973	62.8
$^{133}\text{Ba}$	(1 $\mu\text{Ci}$ )	X (Cs $K\beta 1$ )	34.92	18.2
T = 10.5 yrs.	A = $2.5 \times 10^4$ Bq	X (Cs $K\beta 2$ )	35.82	4.6
		$\gamma$	53.1622	2.14
		$\gamma$	80.9979	32.9

detectors are also needed. The parameters utilized in the definition of the detectors are presented in Table. 3.2.

As it can be observed that all the fundamental requirements for the theoretical efficiency calculations are available and for experimental calculations, the spectrum of various standard radioactive sources whose intensities are described in Table. 3.1 are obtained from XR-100CR Si(Li) Pin detector.

Table 3.2: Parameters used for Detector Calibration provided by Amptek.

Parameter	XR-100CR	XR-100T
Detector Type	Si-Pin	CdTe
Detector Size	13 mm <sup>2</sup>	7 mm <sup>2</sup>
Detector Thickness	300 $\mu$ m	1 mm
Detector Be window thickness	1 mil (25 $\mu$ m)	1 mil (25 $\mu$ m)
Detector Density	2.33 g/cm <sup>3</sup>	6.2 g/cm <sup>3</sup>

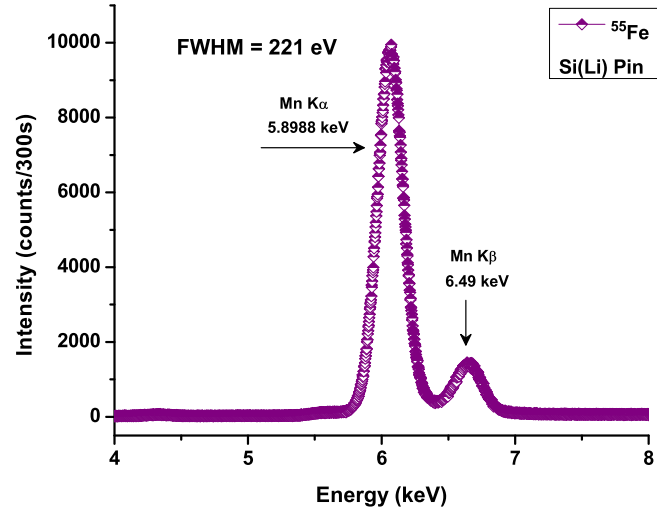


Figure 3.13: Spectrum of  $^{55}\text{Fe}$  obtained from the XR-100CR.

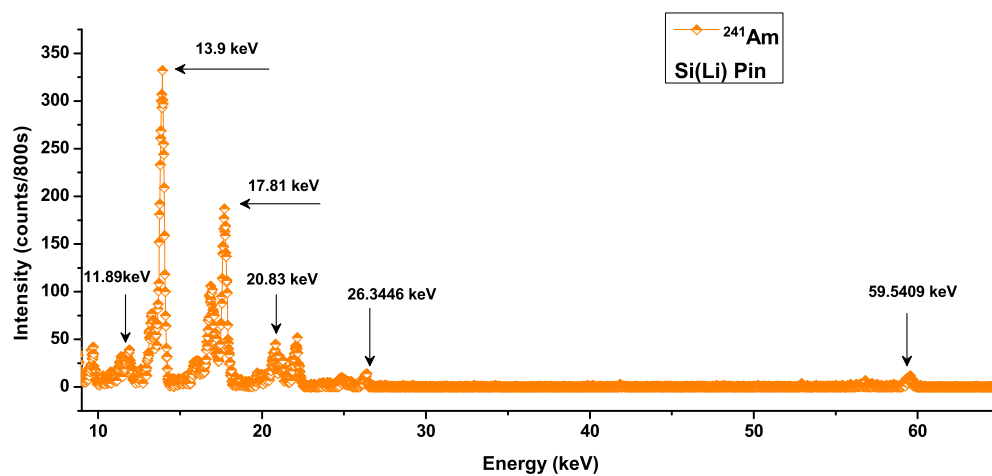


Figure 3.14: Spectrum of  $^{241}\text{Am}$  obtained from the XR-100CR.

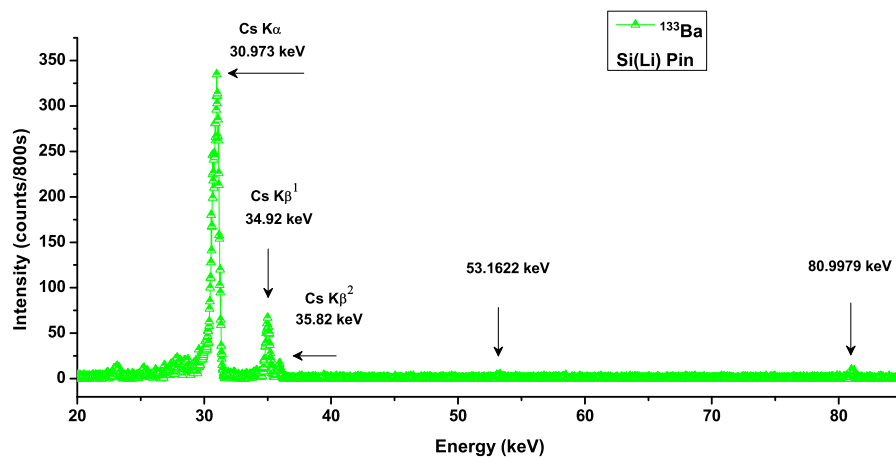


Figure 3.15: Spectrum of  $^{133}\text{Ba}$  obtained from the XR-100CR.

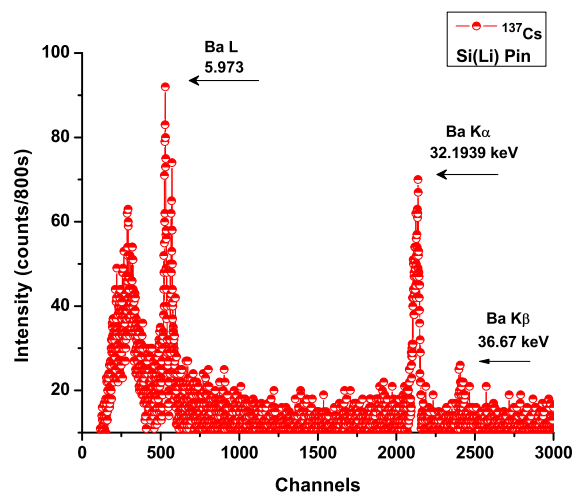


Figure 3.16: Spectrum of  $^{137}\text{Cs}$  obtained from the XR-100CR.

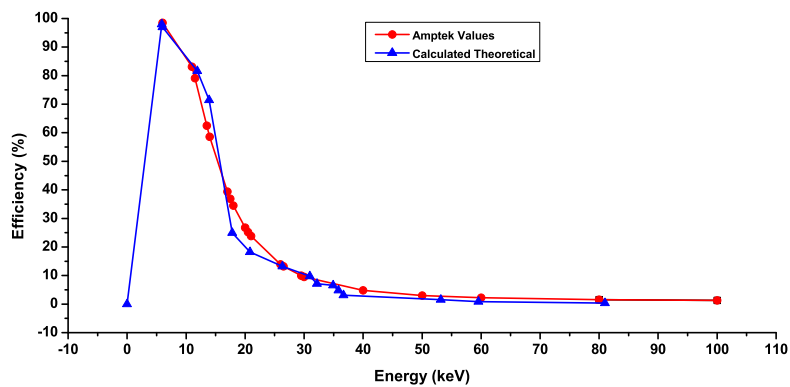


Figure 3.17: Comparison of Amptek Model and Theoretical Calculated Efficiency Curves for XR-100CR.

Table 3.3: Experimental Efficiency results from XR-100CR.

Energy	$\eta_{theoretical}$ (%)	$\eta_{experimental}$ (%)	$I_{trans}$ (counts/sec)	Uncertainty (%)
5.8988	98	82.55	49.47	0.11
6.49	97	79.117	49.47	0.211
11.89	81.5994	40.44	$3.176 \times 10^3$	27.14
13.9	71.4373	23.115	$3.176 \times 10^3$	1.92
17.81	24.959	7.71	$1.6549 \times 10^4$	7.71
20.82	18.2314	5.23	$2.4195 \times 10^4$	5.23
26.34	13.2413	1.207	$3.0144 \times 10^4$	8.87
30.973	9.7804	3.0746	$2.2836 \times 10^4$	10.71
32.1939	7.1143	2.1706	$16.8990 \times 10^4$	3.40
34.92	6.5407	1.3884	$2.2836 \times 10^4$	4.50
35.82	4.78	1.236	$2.2836 \times 10^4$	8.87
36.67	3.1055	2.3685	$17.8141 \times 10^4$	6.69
53.1622	1.5709	0.57208	$2.4519 \times 10^4$	20.89
59.5409	0.8375	0.0851	$3.2621 \times 10^4$	10.71
80.9979	0.355	0.0097	$2.4853 \times 10^4$	18.35

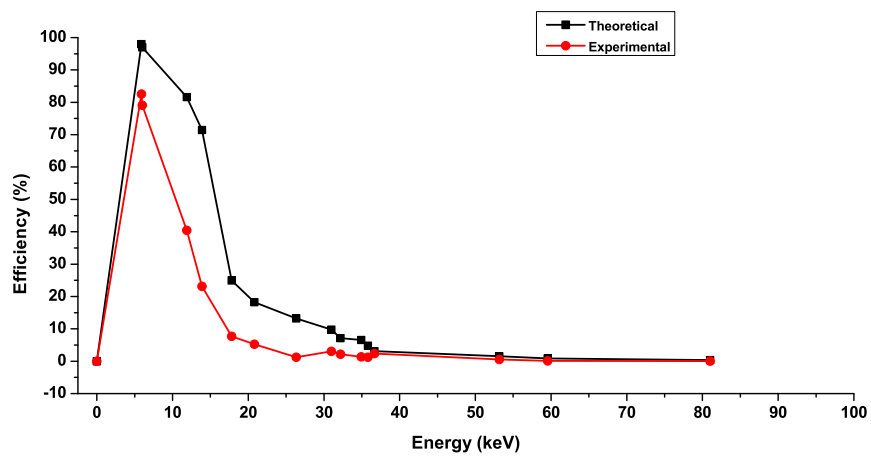


Figure 3.18: Comparison of Experimental and Theoretical calculated efficiency points for XR-100CR.

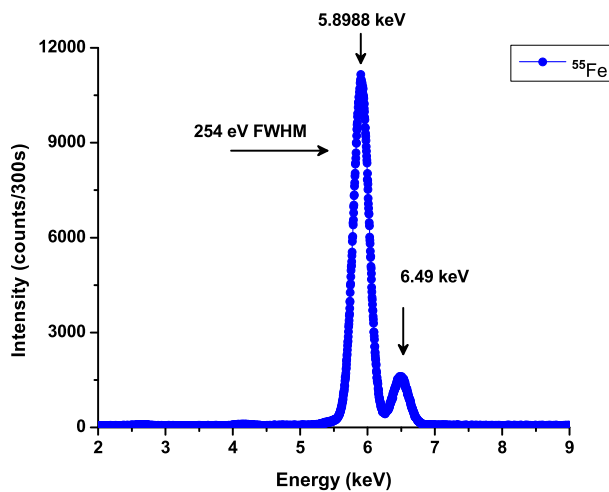


Figure 3.19: Spectrum of  $^{55}\text{Fe}$  obtained from the XR-100T.

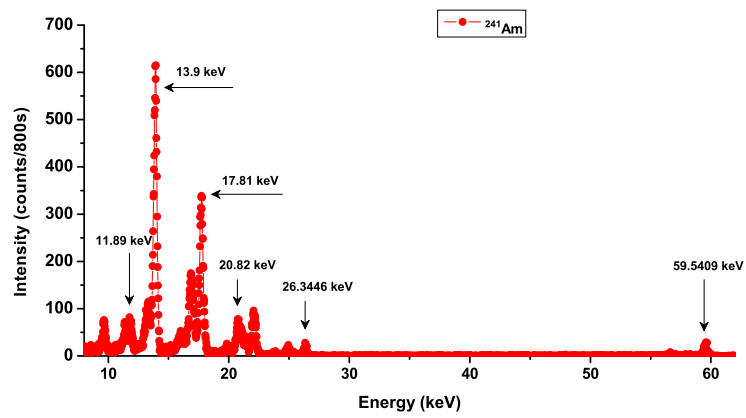


Figure 3.20: Spectrum of  $^{241}\text{Am}$  obtained from the XR-100T.

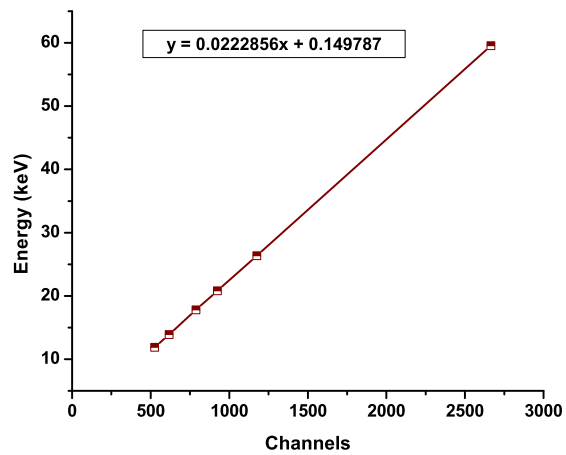


Figure 3.21: Energy Calibration from  $^{241}\text{Am}$  source for XR-100T-CdTe detector.



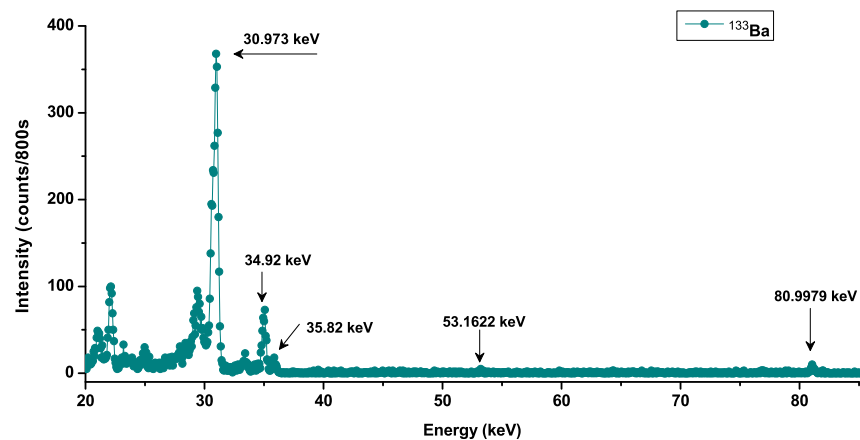


Figure 3.22: Spectrum of  $^{133}\text{Ba}$  obtained from the XR-100T.

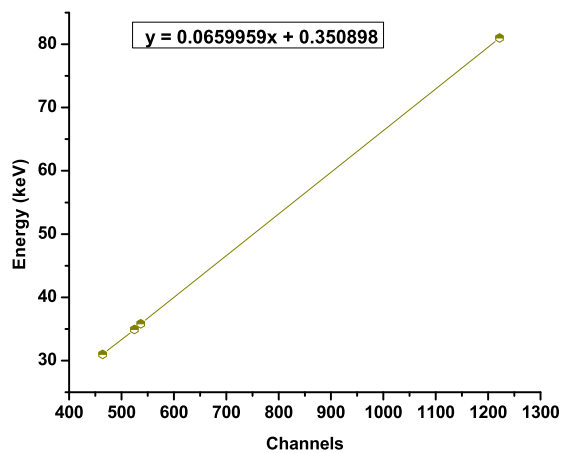


Figure 3.23: Energy Calibration from  $^{133}\text{Ba}$  source for XR-100T-CdTe detector.

Table 3.4: Experimental Efficiency results from XR-100T.

Energy	$\eta_{\text{Amptek}}$ (%)	$\eta_{\text{theoretical}}$ (%)	$\eta_{\text{experimental}}$ (%)	$I_{\text{trans}}$ (counts/sec)	Uncertainty (%)
5.8988	81.44	89.97	65.76	0	0.11
6.49	88.80	85.64	50.9088	0	0.48
11.89	97.79	89.10	21.03	$3.354 \times 10^{-6}$	11.35
13.9	98.57	92.56	36.9	$5.638 \times 10^{-4}$	1.39
17.81	98.57	96.35	16.08	$5.638 \times 10^{-4}$	1.68
20.82	98.95	99.98	15.32	$4.763 \times 10^{-4}$	3.21
26.34	99.09	99.95	11.9108	$3.927495 \times 10^{-4}$	6.00
30.973	99.16	99.89	10.454	$6.560 \times 10^{-6}$	2.10
34.92	99.16	99.05	4.5843	$9.816 \times 10^{-6}$	6.04
35.82	99.21	99.82	4.3917	$9.816 \times 10^{-6}$	5.17
59.5409	97.47	97.845	1.07	570.6	5.21
80.9979	83.60	81.935	0.0195	$3.8422 \times 10^3$	0

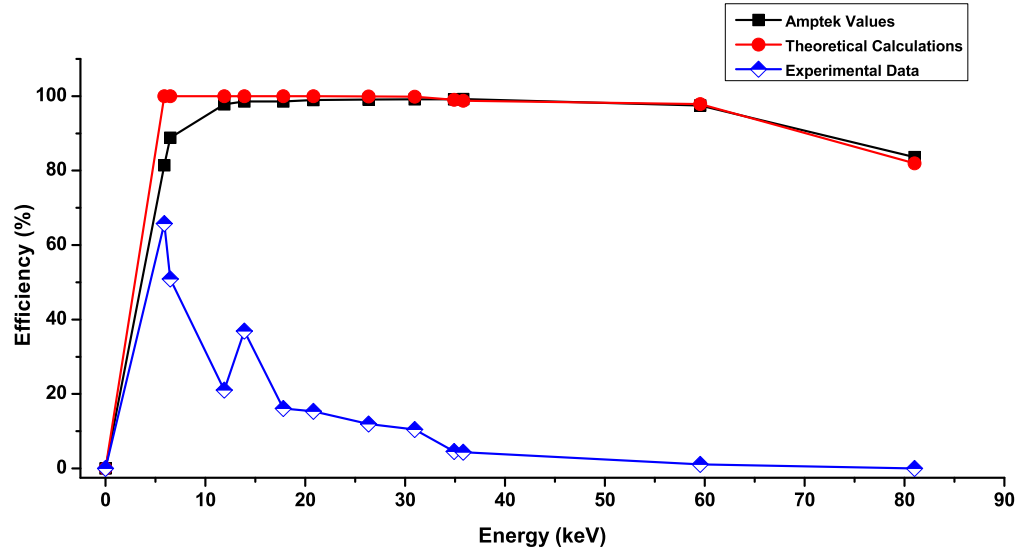


Figure 3.24: Experimental Efficiency points along with the Amptek Model and Theoretical values for a XR-100T-CdTe detector.

### 3.6.7 Escape Peaks

A 1 mm thick CdTe detector has sensitivity up to about 100 keV, with a photopeak efficiency  $>90\%$  to 65 keV. This is far superior to Si detectors, where the efficiency drops off by 20 keV. Photons with incident energy just above these edges undergo photoelectric interactions, leaving the Cd and Te atoms in an excited state. When the atoms transition to the ground level they often emit a characteristic X-ray and depending on the direction, this X-ray may leave the CdTe volume so only a small amount of the incident energy is deposited. Such events lead to fewer full energy events (causing the absorption edges) and more low energy events (below the filter value) than would otherwise occur. This process is responsible for the escape peaks which are well known in spectroscopy. Escape events are more important in CdTe than in Si or Ge due to the much higher energies of the characteristic X-rays. Figure illustrates the events in which the complete energy is deposited, on the left, and those in which a characteristic X-ray escapes, on the right. Photons incident at any one energy  $E_{inc}$ , if greater than the K-edges, will lead to escape events at four lower energies. The fraction of events in each of these escape peaks depends on the probability of X-ray escape, and thus, on the energy of the incident X-rays along with the geometry of the detector [26].

In CdTe, both the Cd and the Te produce both  $K\alpha$  and  $K\beta$  peaks, so each primary photopeak produces four escape peaks and the characteristic energies are 23.2 and 26.1 keV for the Cd  $K\alpha$  and  $K\beta$ , and 27.5 and 31.0 keV for the Te peaks. Figure 3.14 shows the spectrum measured from a  $^{241}\text{Am}$  source, with an Al filter, used to remove the X-ray lines below the 59.5 keV line. The four distinct escape peaks are clearly visible and include a significant fraction of the photopeak events. Spectrum analysis software must correct such effects to obtain an accurate photopeak area. This way it is possible to prevent escape peaks from obscuring real X-rays at this energy, and to avoid misidentifying these as real peaks in the incident energy spectrum.

### 3.7 Si-Pin vs CdTe Comparison

Ideally, as indicated by the manufacturer [13], x-ray detectors either Si-Pin or CdTe as their sensing materials, will have advantages that will be beneficial depending on the applications. The plots, Figs. 3.25, 3.26, and 3.27, show detailed comparison of the efficiency and resolution performance of these detectors. Si-Pin is the detector of choice when dealing with low energies, generally below 25 keV, since it has better energy resolution, better peak to background ratio and lower background counts. To use CdTe as a detector, it is preferred

with high energy x-rays, 25 keV and above, as it has better stopping power compared to Si-Pin at high energies. However there are some trade-offs and overlaps, depending on the details of the application that should be taken into consideration, quite often using an Edisonian approach.

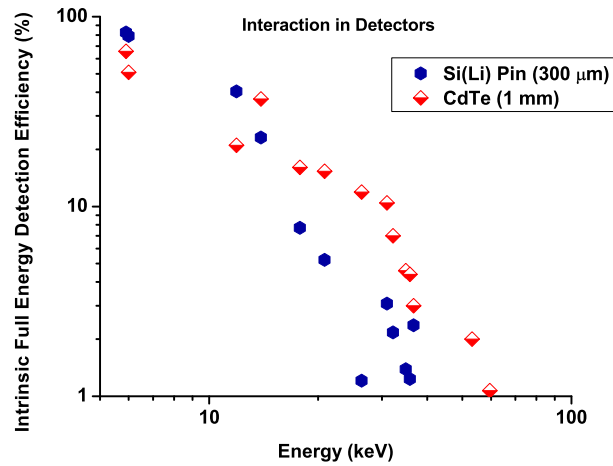


Figure 3.25: Comparison of Intrinsic Full Energy Detection Efficiency vs Photon Energy from XR-100CR and XR-100T.

Fig. 3.25 shows the intrinsic full energy detection efficiency comparison and this efficiency corresponds to the probability that an x-ray will enter the front of the detector and deposit all of its energy inside the detector via the photoelectric effect. As observed in the plot, red line, the Si-Pin detector's efficiency drops at about 20 keV and then it decreases more or less continuously, whereas in

the case of CdTe, the efficiency is lower but its slope is less pronounced until about 40 keV, afterwards the slope has a similar value.

Comparing the output spectra obtained from different detectors, Si-Pin and CdTe, shown in Figs. 3.26 and 3.27, and their respective resolutions in Table 3.5, it is observed that the experimental resolution values calculated for CdTe are lower, compared to the values provided by the manufacturer [13]. Such an aspect highlights the relevance of characterizing the specific detector(s) in use.

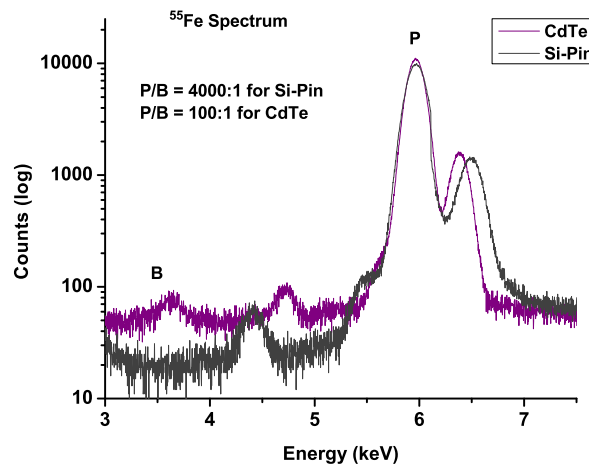


Figure 3.26: Comparison of  $^{55}\text{Fe}$  Spectrum obtained from XR-100CR and XR-100T.

We could venture into providing various reasons to explain the discrepancies in the results observed: damage due to improper use, improper cooling, and

others, but that is not the objective of this study. In principle, it is expected that CdTe has good stopping power, making it efficient enough for high energy detection, close to 100 keV, but our particular detector behave rather unexpectedly, assuming that the expected physical parameters actually correspond to the ones fed to the equations. Only a comparison of elemental concentrations obtained from this and other detectors would dispel any possibility for malfunction. For the Si-Pin detector the correspondence between the values provided by the manufacturer and the ones measured is much better, and expected in a working device. Once again, the discrepancy stresses the importance of efficiency characterization for accurate elemental analysis and any possibility for malfunction. For the Si-Pin detector the correspondence between the values provided by the manufacturer and the ones measured is much better, and expected in a working device. Once again, the discrepancy stresses the importance of efficiency characterization for accurate elemental analysis.

Table 3.5: Resolution (eV FWHM) Characteristics

Line	Si (Amptek)	Measured Si	CdTe (Amptek)	Measured CdTe
5.9 keV	219	221	240	254
13.95 keV	225	252	390	297
59.54 keV	452	113	602	211

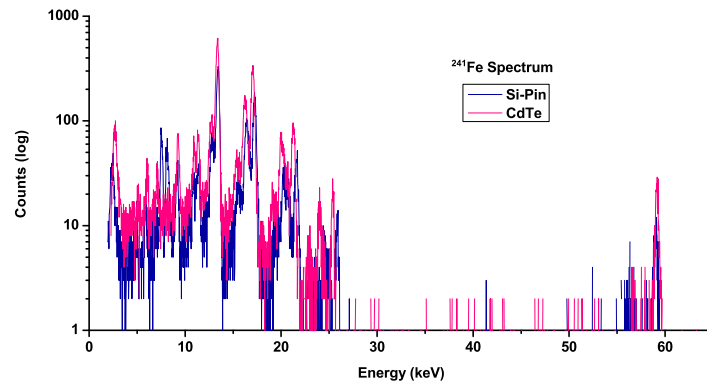


Figure 3.27: Comparison of  $^{241}\text{Am}$  Spectrum obtained from XR-100CR and XR-100T



# Chapter 4

## XRF measurements

### 4.1 Energy Dispersive XRF Technique

XRF relies on analytical methods characterized by simple or no sample preparation, and by the non-destructive, high-speed qualitative and quantitative analysis of a wide range of elements and concentrations.

When an X-ray excitation source strikes a sample, the X-ray is absorbed by the atom by transferring all of its energy to an inner electron. If the X-ray has sufficient energy, the electrons are ejected from inner shells, creating vacancies that present an unstable condition within the atom. When the atom returns to its stable condition the electrons from outer shells are transferred to inner shells, giving off a characteristic X-ray photon whose energy is the difference of

the two binding energies of the corresponding shells.

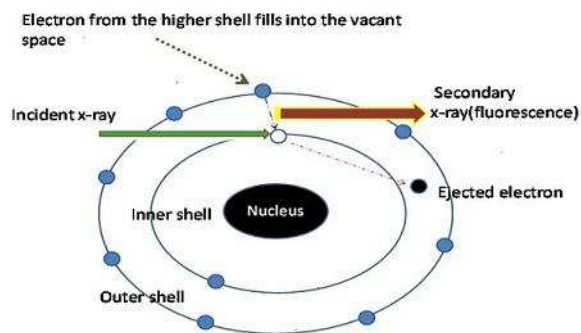


Figure 4.1: Illustration of X-ray Fluorescence

For a particular element there is also a particular fluorescent emission, the number of photons per unit time is related to the amount of that element in the sample. The counting rates for all detectable elements within a sample are obtained by counting, for a preset amount of time. Table. 4.1 lists the K-edge emission energies of several elements that will be discussed in this chapter. An absorption edge refers to a sudden change in the attenuation coefficient of photons occurring at photon energy just above the binding energy of the energy shell of interest.

By determining the energy of the X-ray peaks in a sample's spectrum, and by calculating the count rate of the various elemental peaks, it is possible to qualitatively establish the elemental composition of the samples and further analysis of the spectrum can turn into a quantitative measure of the concen-

Table 4.1: Emission energies of some metals [44]

Atomic number	Element	$K\alpha$ (keV)	$K\beta$ (keV)
24	Cr	5.41	5.95
26	Fe	6.40	7.06
29	Cu	8.05	8.90
30	Zn	8.64	9.57

tration of these elements. X-ray fluorescence can be measured and quantified in two ways: wavelength dispersive and energy dispersive XRF. Wavelength dispersive XRF uses a crystal to separate the various wavelengths. For every angle of incident radiation, the only wavelength reflected to the detector is the one that conforms to Bragg's formula,  $2d\sin\theta = n\lambda$  [8].

The energy dispersive XRF method, is more commonly used and consists of allowing all wavelengths enter the detector at once. The detector registers an electric current proportional to the photon energy. These pulses are separated electronically using a multichannel analyzer, MCA. The resolution and detection limit are better for wavelength dispersive XRF while energy dispersive XRF has the advantages of simplicity of instrumentation and less acquisition time. Choosing optimal acquisition conditions for XRF analysis is a complex

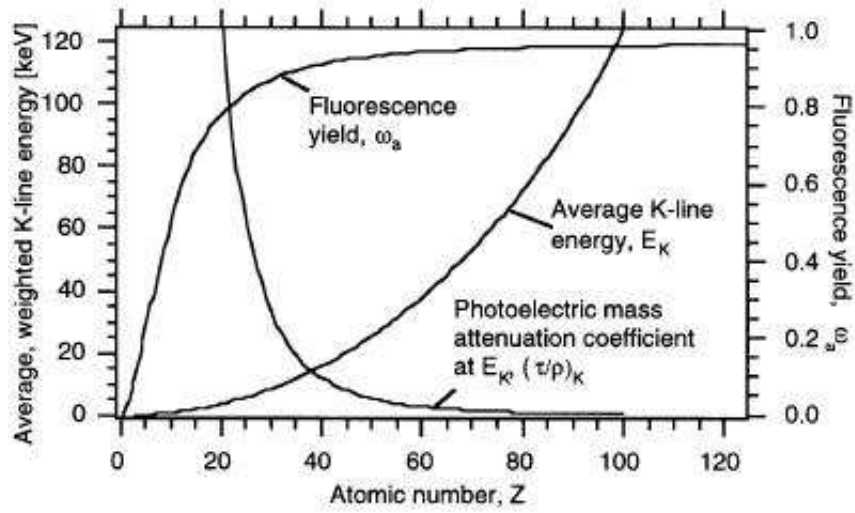


Figure 4.2: Here we show three lines, one referring to the fluorescent yield, which increases with atomic number, another one to the photoelectric mass attenuation coefficient, which decreases with atomic number, and the average K-line energy, which increases with atomic number.

problem. There must be a significant source peak (excitation peak) above the absorption edge energy of the element of interest. This edge may be either the K- or L-edge, depending on which one is within the measurable range of the detector. The closer the source energy is to the absorption edge, the higher the intensity and sensitivity will be for the element of interest. Another fundamental aspect is that the background x-rays in the neighborhood of the energy region of interest should be reduced as much as possible.

An important aspect to highlight is that the parameters discussed above actually work in opposition to each other; i.e. the best sensitivity is often achieved when the background is highest, and the background is lowest when the sensitivity is worst [10]. Thus a compromise between these two principles is to be found, quite often through a trial-and-error basis. A typical XRF spectrum from an irradiated sample will display multiple peaks of different intensities, each peak corresponding to a particular element. The area under each characteristic peak reflects the elemental concentration. Conventional XRF detection limits can be obtained with an accuracy within a microgram-per-gram (ppm) level, certainly all depending on the specific features of the instrumentation used. Intensity data are converted to analytical concentration by use of calibration curves or mathematical relationships derived from measurements on standards [45].

Using the equations described in [45] and [46], we can calculate the net x-ray intensities emitted by each element from a specimen of known composition when a polychromatic beam irradiates it, which is given by

$$I_i = f(C_i, C_j, C_k, \dots, C_N) \quad (4.1)$$

where  $I$  and  $C$  are the net intensity and the concentration of  $N$  elements present

in the sample. This method is of vital importance, because it enables calculating what we measure, which are the line intensities. The Sherman equations [45, 46] can be reduced after doing some algebraic manipulations, in the following mathematical form,

$$R_i = C_i \left( \frac{1 + \sum_j \epsilon_{ij} C_j}{1 + \sum_j \alpha_{ij} C_j} \right), \quad (4.2)$$

where

$$\epsilon_{ij} = \frac{\sum W_i(\lambda_k) \delta_{ij}(\lambda_k)}{\sum W_i(\lambda_k)}, \quad (4.3)$$

$$\alpha_{ij} = \frac{\sum W_i(\lambda_k) \beta_{ij}(\lambda_k)}{\sum W_i(\lambda_k)}. \quad (4.4)$$

where the weighting factor,  $W_i(\lambda_k)$  can be written as

$$W_i(\lambda_k) = \left[ \frac{\mu_i(\lambda_k) \cdot I_0(\lambda_k) \Delta \lambda_k}{\mu_i^* \cdot [1 + \sum C_j \beta_{ij}(\lambda_k)]} \right], \quad (4.5)$$

Eq. 4.2 is the relative intensity equation, which shows that  $R_i$  is proportional to the concentration  $C_i$ . The numerator of the multiplicative factor of  $C_i$ , contain indirectly, through  $\epsilon_{ij}$ , the electron density of the material,  $\delta_{ij}$ . The denominator contains the absorption coefficients  $\beta_{ij}$  of each element  $j$ , again, in an indirect way, through  $\alpha_{ij}$ . The method of the Sherman equations [45, 46]

is also known as method of Fundamental Parameters. The required parameters are fed to the analysis software and by taking account of the absorption and electron densities, we get a fit between the relative intensities and concentrations which is the final aim of the present study.

## 4.2 Elemental Analysis using a CdTe XR-100T

In the present investigations, the X-ray fluorescence technique has been employed to study, qualitatively, three types of metallic samples: aluminum, lead and nickel. Typically, fluorescence analysis experiments have been performed using radioactive sources [39], Americium ( $^{241}\text{Am}$ ) [38] and Cobalt ( $^{57}\text{Co}$ ) [40]. The source activities are  $10^5$  Bequerel (Bq) (0.1 mCi) which required data collection times of about one hour. The alternative of using a pyroelectric crystal [12], as has been noted elsewhere [14], offers the possibility of a higher-activity equivalent source,  $10^7$  Bq, that can be powered as required and is fairly portable, that additionally, has been configured in a compact setup that encloses a solid state detector, either Si-Pin or CdTe, inside a box made up of polyoxymethylene, known with the DuPont brand name, delrin.

Fig. 4.3 contains a schematic of the experimental setup used. The X-ray source is an Amptek COOL-X pyroelectric generator. The detector, which has

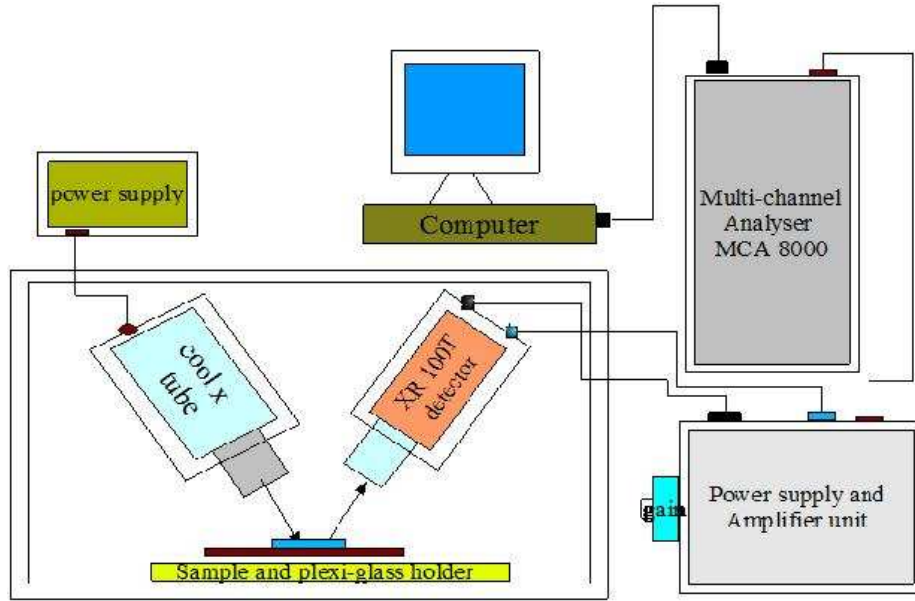


Figure 4.3: Experimental Setup

a resolution of 200 eV at 22 keV, is of the solid state type, a 7 mm<sup>2</sup> CdTe crystal from Amptek, model XR-100T which is connected to the Amptek PX-2T module that contains the pre-amplifier, amplifier and power supply. The sample is mounted at 45° to the detector and the source. The geometry used provides a compact coupling between the source, sample and detector. The obvious advantage associated with the geometry chosen lies in the reduction of Compton scattered background, since the cross-section for scattering is a minimum around 90°. The detector and pyroelectric generator are Peltier cooled and thus affixed to 6-mm thick aluminum plates serving as heat sinks.



The output from the PX-2T is sent to an MCA, Amptek pocket MCA 8000A, controlled via the serial port of a computer where all information is recorded. Detector sample and source are enclosed in a polyoxymethylene enclosure, of 20-mm thick walls, that serves as a radiation shield, to prevent the operator from accidental radiation exposure.

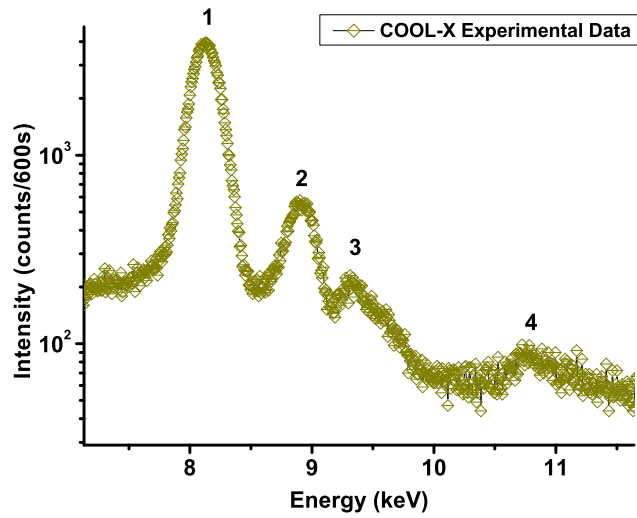


Figure 4.4: Spectrum obtained from the Pyro-electric Generator

The spectrum produced by the source can be seen in Fig. 4.4. The narrower and more prominent features are the characteristic X-ray lines excited during the warm-up and cool-down cycles: (1) Cu  $KL_3$  = 8.048 keV and Ta  $L_3M_5$  = 8.146 keV, (2) Cu  $KM_{2b}$  = 8.9053 keV, (3) Ta  $L_2M_4$  = 9.3429 keV and (4) Ta

$L_2N_4 = 10.895$  keV; using the IUPAC nomenclature [43]. The Cu  $KL_3$  and Ta  $L_3M_5$  lines are not resolved and represent the most intense line observed.

The characteristic lines, in Fig. 4.4, are also used for calibration purposes. The energy calibration is done according to the Eq. 3.1. The full spectral output is directed at the sample to be analyzed for a predetermined time interval of 600 s. Samples of Nickel foil (99.95% purity, 0.009 mm thick produced by Goodfellow), aluminum (Al) and lead (Pb) scrap plates were irradiated. The Nickel (Ni) foil was placed in a self-supported holder that did not have the polymethyl methacrylate backing. The Pb and Al plates were 15 mm and 10 mm thick, respectively, therefore opaque to the X-rays.

Ni foil was irradiated for 600 secs and the spectrum produced was observed in Fig. 4.5. Lines (1) Co  $KM_2 = 7.649$  keV, Co  $KM_3 = 7.649$  keV, Ni  $KL_2 = 7.461$  keV and Ni  $KL_3 = 7.478$  keV, are not resolved individually, but given the FWHM, it is relevant to consider the Co lines. Co is a common impurity found in Ni. Line (2), includes Cu  $KL_3 = 8.048$  keV, Ta  $L_3M_5 = 8.146$  keV, Ni  $KM_2 = 8.265$  keV, Ni  $KM_3 = 8.265$  keV. Cu and Ta lines are not unexpected since they are contained in the source. Line (3) Zn  $KL_3 = 8.639$  keV, indicates the presence of another impurity in the Ni foil.

In Fig. 4.6, the spectral content of a Pb plate, irradiated for 600 secs, shows

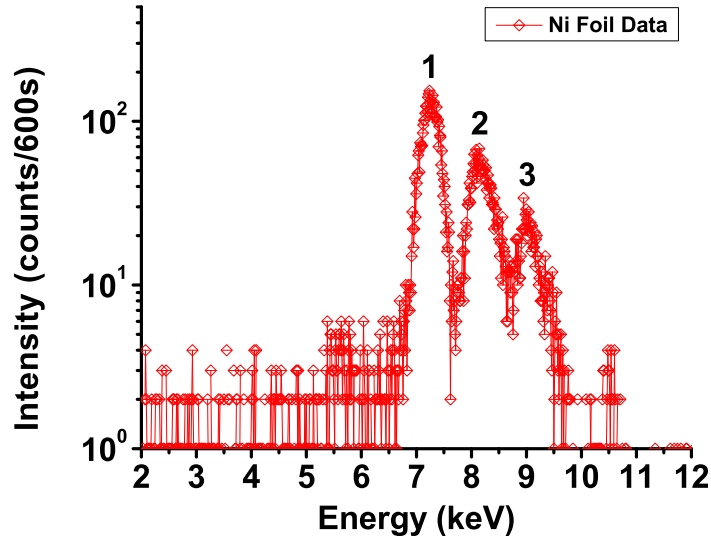


Figure 4.5: Spectrum from Ni foil after irradiation for 600s

four statistically resolvable characteristic lines. Line (1)  $\text{Cu } KL_3 = 8.048 \text{ keV}$ ,  $\text{Ta } L_3M_5 = 8.146 \text{ keV}$ . Line (2) is formed by the superposition of  $\text{Zn } KL_2 = 8.616 \text{ keV}$ ,  $\text{Zn } KL_3 = 8.639 \text{ keV}$ ,  $\text{Cu } KM_2 = 8.905$ ,  $\text{Cu } KM_3 = 8.905 \text{ keV}$ , while lines (3)  $\text{Pb } L_3M_4 = 10.450 \text{ keV}$ , and (4)  $\text{Pb } L_1M_2 = 12.307 \text{ keV}$  are clearly defined, as it appears by their 200 eV FWHM. A peak appears to be located at 6.7 keV, but statistically it was not possible to assign an elemental line to it.

The XRF spectrum from Al plate, Fig. 4.7, was recorded at 600 s. The peak,  $\text{Al } KM_3 = 1.554 \text{ keV}$ , is not easily discernible due to its proximity to

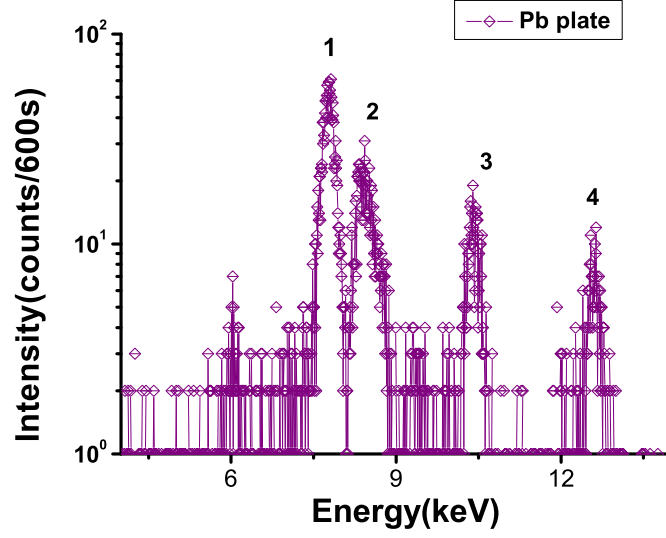


Figure 4.6: Spectrum from Pb plate irradiated for 600 s

the Line (1) Ta  $M_5N_7 = 1.710$  keV peak, which is a source peak and also contaminates the Al plate spectrum. The signal at Line (2) corresponds to Fe  $KL_2 = 6.391$  keV, and that at Line (3) to Gd  $L_2M_4 = 6.713$  keV. Gadolinium is often added to Al alloys to improve the physical properties of the alloy, like strength or workability. Other source components are also found at Line(4) Cu  $KL_2 = 8.028$  keV, Cu  $KL_3 = 8.028$  keV, and Ta  $L_3M_5 = 8.146$  keV. Finally, Fig. 4.7, one more can be identified Line (5) Zn  $KL_2 = 8.616$  keV, Zn  $KL_3 = 8.639$  keV, Cu  $KM_2 = 8.905$  keV, and Cu  $KM_3 = 8.905$  keV; source peaks closely overlap with Zn peaks. Statistically, no further peaks were identified at least within the collection times set.

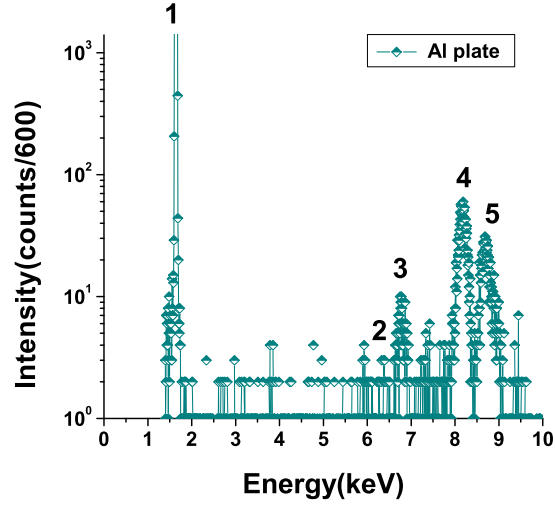


Figure 4.7: Spectrum from Al plate irradiated for 600s

The spectral content in all samples irradiated, has been identified by manually exploring the database in the X-ray data booklet [44], from the Center of X-ray Optics and Advanced Light Source. The results obtained from the analysis of the individual peaks of the three samples are given in Table. 4.2.

The counting times employed in the set of experiments presented, are con-

Table 4.2: Results from irradiation of metallic samples.

Sample	Major Elements
Ni Foil	Ni, Co, Zn
Pb Plate	Pb, Zn
Al Plate	Al, Zn, Fe, Gd

siderably below, in magnitude, than those presented when using radioactive sources, but about six times larger than commercially available equipment already configured for XRF analysis, like the X-MET 300 TXV+ from Oxford Instruments, where the beam is more collimated and there is a considerable shorter, about three-fold, sample-to-source distance.

### **4.3 Semi-Quantitative Analysis using a Si(Li) XR-100CR detector**

The technique and setup used in the previous analysis as in Fig. 4.3 is again employed, the only change being the use of Si(Li) XR-100CR detector instead of the CdTe XR-100T detector and the samples used for this process are Standard Reference Materials (SRM) namely 1240c Aluminum Alloy 3004, C2417 Lead Base Alloy and 1159 Electronic and Magnetic Alloy.

The x-ray generator used in this process is COOL-X and its details are discussed in Section. 3.1 and Appendix A.1. The fluorescence x-rays emitted from the sample were detected by an XR-100CR Si-Pin detector [13] with  $13\text{mm}^2$  effective detection area,  $300\mu\text{m}$  thick and a 219 eV energy resolution for 5.9 keV x-rays. The experimental configuration is as described in Sec. 4.2. The cal-

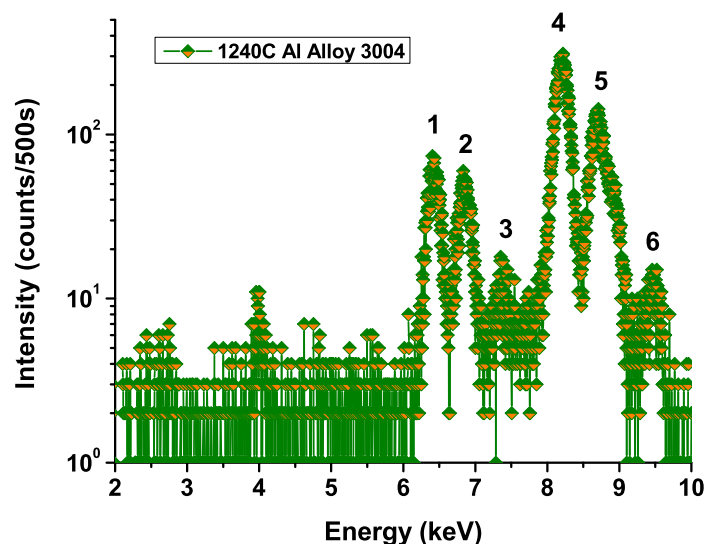


Figure 4.8: X-ray Fluorescence spectrum from 1240c Aluminum Alloy for 500s  
 ibrated output spectrum obtained from the COOL-X through the XR-100CR  
 detector was utilised for the reference data. Although the power of x-ray output  
 was a few orders of magnitude lower than the conventional x-ray tubes, several  
 elements like Fe, Zn, Ba and Pb were detected. Light elements such as Mg and  
 Al are not detected because the absorption of fluorescent x-rays with such an  
 energy in air.

The SRM 1240C Aluminum Alloy 3004 is produced by the National Institute  
 of Standards and Technology and are intended primarily for use in evaluating  
 methods of analysis, one of which is XRF. The 1240C has been irradiated for

Table 4.3: Identification of peaks in 1240C Al alloy 3004

No	Element	Line	Energy(keV)
1	Mn	$KM_3$	6.4904
	Fe	$KL_2$	6.3909
	Fe	$KL_3$	6.4039
2	Ga	$L_2M_4$	6.713
	Fe	$KM_2$	7.058
	Fe	$KM_3$	7.058
3	Ni	$KL_2$	7.4609
	Ni	$KL_3$	7.4781
4	Cu	$KL_3$	8.028
	Ta	$L_3M_5$	8.146
	Ni	$KM_3$	8.265
5	Zn	$KL_2$	8.616
	Zn	$KL_3$	8.639
	Cu	$KM_2$	8.905
6	Ta	$L_2M_4$	9.342
	Zn	$KM_3$	9.572



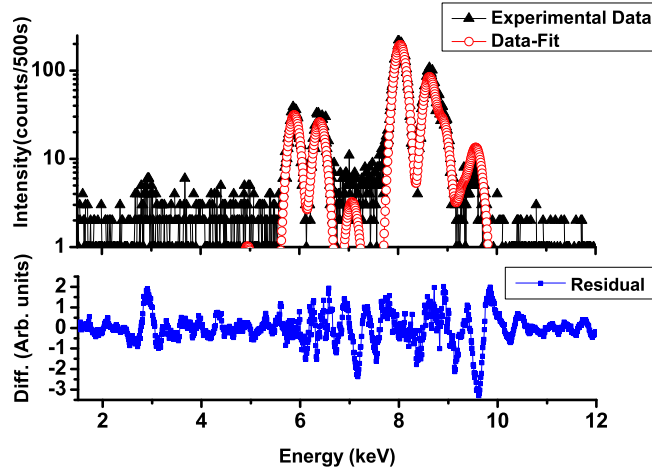


Figure 4.9: Comparison of experimental and fitted data for 1240C. The black triangles represent the experimental data, the red circles represent the fit, and the blue squares indicate the residuals.

Table 4.4: Relative Concentrations of 1240C Al Alloy 3004

Z	Symbol	Area counts	Yield $/\mu\text{ng}/\text{cm}^2$	% Stat. Error	%Fit Error	LOD counts
12	MgK	5.8	10478	136.30	121.90	16.2
14	SiK	0	7448	0	0	15.3
22	TiK	0	1307	0	0	18.7
23	V K	17.2	1032	50.97	55.36	12.5
25	MnK	532.6	663.2	4.23	5.29	17.9
26	FeK	390.6	539.4	5.84	6.66	31.7
28	NiK	0	346.8	0	0	34.0
29	CuK	3258.9	262.0	1.66	2.40	52.1
30	ZnK	1448.4	207.6	2.85	3.51	39.4
31	GaK	21.9	158.1	80.95	81.88	35.3
73	TaLA	210.4	99.87	52.77	31.86	246.1

period of 500s and the respective spectrum is obtained and the calibrated reference data available from the COOL-X is used to evaluate the different elemental energy peaks present in it. Apart from the energy values obtained from the source we have observed individual peaks from Fe, Mn, Zn and Ni. The Si peak can not be detected with the current setup. XRF spectra of the representative sample 1240C Aluminum Alloy 3004 are shown in Fig. 4.8. The results obtained from the analysis of the individual peaks of the Aluminum Alloy 3004 SRM are given in Table 4.3. Now considering the equations which are described earlier in Sec. 4.1, we found the relative intensities and the concentrations of the 1240c alloy by taking account of the respective parameters. Discrepancies between fit and experiment are greater whenever elemental spectral lines are dealt with, which is quite normal. The relative concentrations have been presented in Table. 4.4 and also their residuals are shown, blue line.

Using the energy-dispersive x-ray fluorescence method, the C2417 Lead Base Alloy has been irradiated for 500s. The semi-quantitative analysis has been performed and the characteristic x-rays energies of different elements have been detected. It is know that this alloy contains some residual elements like Sb, As, Bi, but these elements have not been detected because of their low concentration. A typical XRF spectrum of C2417 is shown in Fig. 4.10. The elements

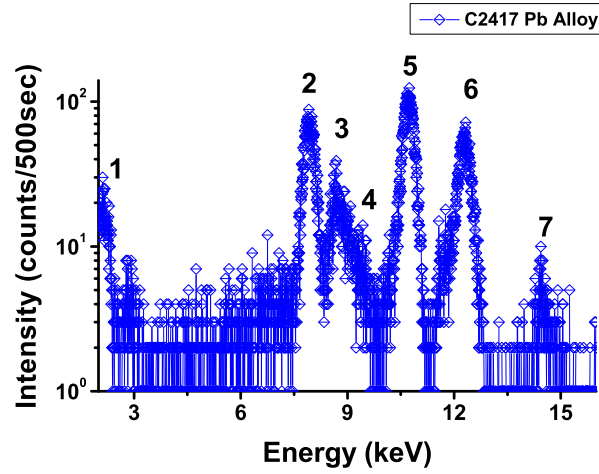


Figure 4.10: Spectrum from C2417 Lead Base Alloy for 500s

are identified and presented in Table 4.5.

The peaks observed in C2417 are mostly those of Pb and from the source itself. The concentrations have been calculated and been tabulated in Table 4.6.

The 1159 EM alloy was irradiated for 500 s, and the output detected using the Si(Li) XR-100CR detector. Lines of different elements like Mn, Fe, Co and Ni are detected. Additionally the peaks of Cu and Ta, both from the the COOL-X can be seen. The spectrum of 1159 EM alloy is shown in Fig. 4.13 and their intensities and concentrations are presented in Table 4.8.

The spectral content in all samples irradiated, has been analyzed by using

Table 4.5: Identification of peaks in C2417 Pb Alloy

No	Element	Line	Energy(keV)
1	Pb	$M_5N_6$	2.3428
2	Cu	$KL_3$	8.028
	Ta	$L_3M_5$	8.146
3	Cu	$KM_2$	8.905
4	Ta	$L_2M_4$	9.342
5	Pb	$L_3M_5$	10.5512
6	Pb	$L_2M_4$	12.6144
7	Pb	$L_2N_4$	14.7648

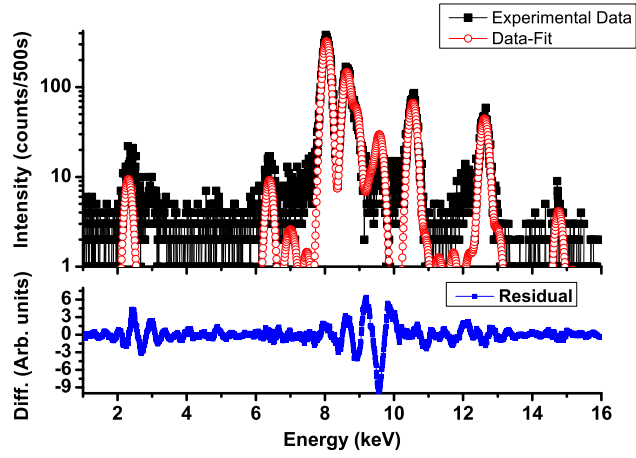


Figure 4.11: Comparison of experimental and fitted data for C2417. The black squares represent the experimental data, the red circles represent the fit, and the blue squares indicate the residuals.

Table 4.6: Relative Concentrations of C2417 Pb base Alloy

Z	Symbol	Area counts	Yield $/\mu/\text{ng}/\text{cm}^2$	% Stat. Error	%Fit Error
13	AlK	0	2483	0	0
16	S K	146.7	3680	12.70	13.25
20	CaK	12.8	1089	66.80	77.02
25	MnK	10.6	960.6	114.83	110.96
26	FeK	145.5	957.5	11.31	12.20
27	CoK	25.6	909.3	56.15 7 57.63	
28	NiK	23.5	904.6	85.56	82.95
29	CuK	5227.6	824.5	1.35	1.68
30	ZnK	2433.8	787.4	2.17	2.46
33	AsK	124.2	554.4	35.72	30.66
73	TaLA	353.7	328.6	43.93	15.61
82	PbLA	1412.4	210.1	3.40	4.42
83	BiLA	0	200.5	0	0

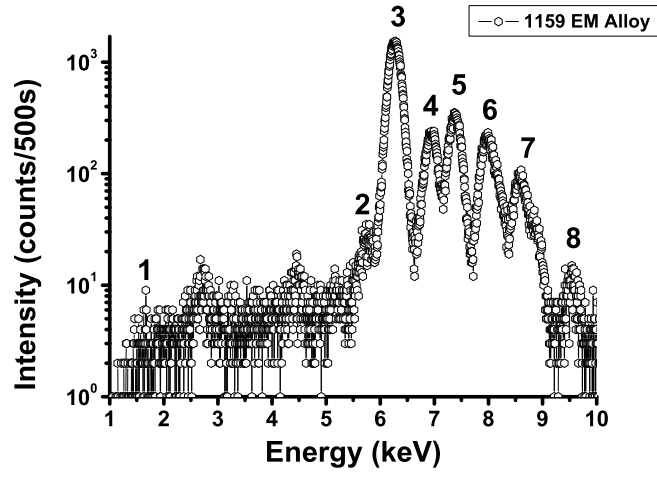


Figure 4.12: Spectrum of 1159 EM Alloy when irradiated for 500s

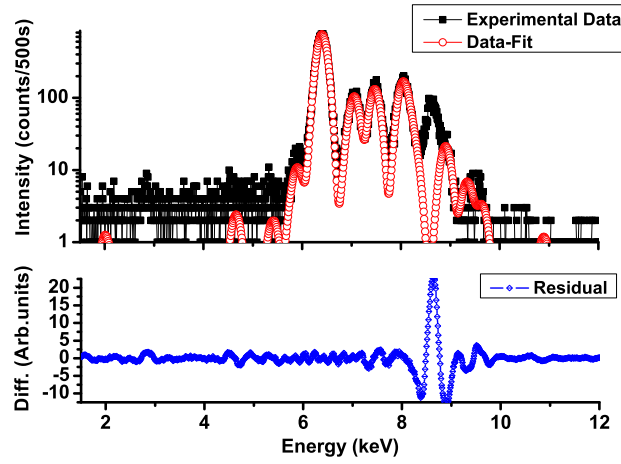


Figure 4.13: Comparison of experimental and fitted data for 1159. The black squares represent the experimental data, the red circles represent the fit, and the blue squares indicate the residuals.

Table 4.7: Identification of peaks in 1159 EM Alloy

No	Element	Line	Energy(keV)
1	Si	$K M_2$	1.8359
2	Mn	$K L_2$	5.8876
	Mn	$K L_3$	5.8987
3	Fe	$K L_2$	6.3909
	Fe	$K L_3$	6.4039
	Mn	$K M_2$	6.4904
4	Co	$K L_3$	6.9303
	Fe	$K M_2$	7.058
	Fe	$K M_3$	7.058
5	Ni	$K L_2$	7.4609
	Ni	$K L_3$	7.4781
	Co	$K M_2$	7.649
6	Cu	$K L_3$	8.028
	Ta	$L_3 M_5$	8.146
	Ni	$K M_3$	8.265
7	Cu	$K M_2$	8.905
8	Ta	$L_2 M_4$	9.342

the PyMca Software [30] and the peaks are identified by manually exploring the database in the X-ray data booklet[44], from the Center of X-ray Optics and Advanced Light Source.

Table 4.8: Relative Concentrations of 1159 EM Alloy.

Z	Symbol	Area counts	Yield $/\mu\text{ng}/\text{cm}^2$	Filter Trans. (-5)	% Stat. Error	%Fit Error	LOD counts
14	SiK	0	7448	4696	0	0	19.2
15	P K	18.2	5958	13191	51.69	65.86	14.9
16	S K	11.5	5033	25681	82.18	101.47	16.4
24	CrK	29.3	844.3	88591	42.92	42.51	14.7
25	MnK	145.5	663.2	91053	14.40	17.76	31.9
26	FeK	11923.3	539.4	92943	0.78	8.25	34.6
27	CoK	72.2	421.0	94391	72.85	65.38	141.4
28	NiK	2131.0	346.8	95514	2.10	8.98	28.7
29	CuK	2579.9	262.0	96390	2.14	9.09	67.4
73	TaLA	372.1	99.87	96517	27.77	17.56	218.6

## 4.4 Comparison of Results with XMET 3000

### TXV+

The Standard Reference Materials which are used for the semi-quantitative analysis using XR-100CR are now analyzed using the XMET 3000 TXV+, an x-ray tube based XRF alloy analyzer. This analyzer is accompanied with a personal data analysis device (PDA) that contains an alloy library to enable quick *in situ* analyses.

The XMET 3000 TXV+ is professionally used for metal scrap sorting and analysis, quality control and material verification, and even measurement of



samples with environmental impact. The XMET 3000 TXV+ uses an x-ray tube of max output of 40kV, 7 $\mu$ A with an Ag source. The detector contained in the compact enclosure is a high resolution Peltier cooled Si-Pin, Fig. 4.14.



Figure 4.14: To the left we have the XMET 3000 TXV+ with the nozzle pointing vertically upward, and to the right we see the diaphragm pump, used to evacuate the nozzle of the XMET to allow detection of low energy fluorescent peaks. On the right we can also observe the PDA.

Typically a measurement with the XMET can take as little as 15 s, certainly depending on the elements of interest and required accuracy. The measurement in this present study are done using the Empirical Calibrations method, that is, with calibrations done *a priory* by the manufacturer using samples of known elemental concentration. The database of the analyzer contains 25 elements between Ti and U. In the present work, we compare the elemental concentration

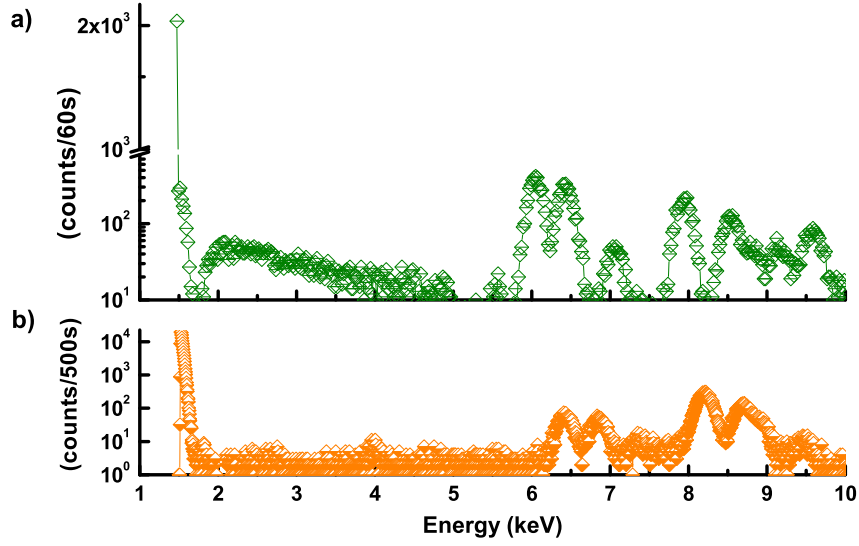


Figure 4.15: (a) Spectrum of 1240C Al Alloy obtained from XMET for 60 s, and (b) spectrum obtained from XR100CR.

of the SRMs measured with the XMET and those obtained in Sec. 4.3.

The counting times employed in the set of experiments presented, are considerably below, an order of magnitude (60 s), than those presented when using the pyroelectric source which is 500 s. As described earlier, the time required by the XMET is lesser due to collimation, detector efficiency and geometrical configuration.

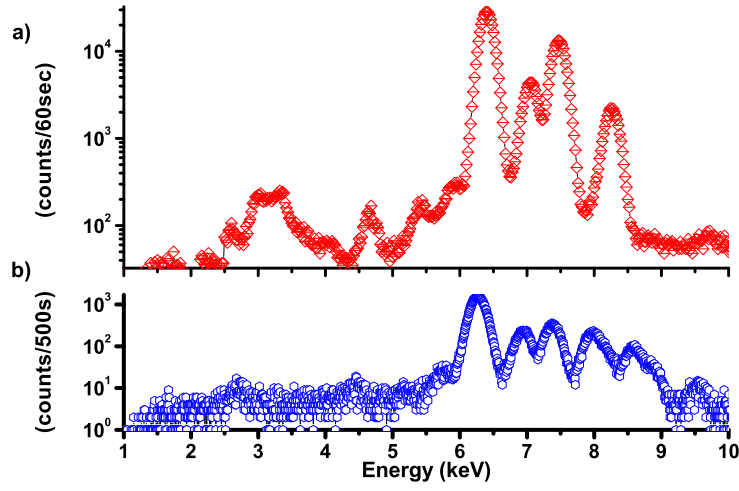


Figure 4.16: (a) Spectrum of 1159 EM Alloy obtained from XMET for 60 s, and (b) spectrum obtained from XR100CR.

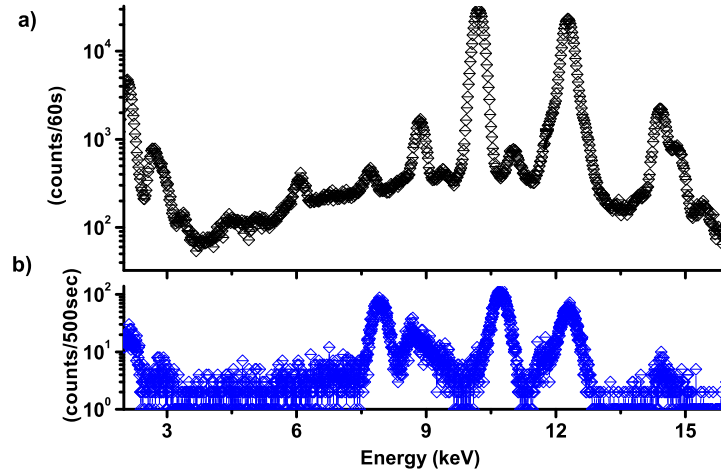


Figure 4.17: (a) Spectrum of C2417 Alloy obtained from XMET for 60 s, and (b) spectrum obtained from XR100CR.

Table 4.9: Comparison of mass fraction values for 1240C Al Alloy 3004.

Constituent	NIST Certified Values (mass fraction %)	XMET (value %)
Fe	0.501	0.44
Cu	0.1484	0.078
Mn	1.268	> 1.11
Mg	1.110	--
Ni	0.00434	< 0.01
Ga	0.0181	—

Table 4.10: Comparison of mass fraction values for 1159 EM Alloy 3004

Element	NIST Certified Values (% by weight)	XMET (value %)
Si	0.32	--
Fe	51.0	50.89
Cu	0.038	0.017
Mn	0.30	0.21
Mo	0.01	0.0029
Ni	48.2	> 48.69
Cr	0.06	< 0.13
Co	0.022	0.01

Table 4.11: Comparison of mass fraction values for C2417 Pb Alloy 3004

Element	NIST Certified Values (% by weight)	XMET (value %)
Pb	—	92.7
Sb	0.010	—
As	0.011	—
Bi	0.01	0.21
Cu	0.01	—
Ag	0.01	< 1.3

## Chapter 5

### Conclusion

In the present work, we have studied the response characteristics of an EDXRF system and the discrepancies of energy, efficiency and resolution of the EDXRF system operating in the energy, 5-60 keV, were discussed. We presented the operational characteristics of the portable pyroelectric x-ray generator, COOL-X, and the application of the calibrated response spectrum to the elemental analysis of some metallic alloys. We studied the efficiency response characteristics of the Si-PIN XR-100CR semiconductor detector to low energy photons. The photopeak efficiency was determined experimentally by using gamma-emitting radioisotopes  $^{55}\text{Fe}$ ,  $^{241}\text{Am}$ ,  $^{137}\text{Cs}$  and  $^{133}\text{Ba}$  and compared against a theoretical efficiency curve. The results showed agreement with the overall tendency pro-

duced by the manufacturer. This gives a good estimation of the Si(Li)intrinsic efficiency and represents an initial step towards setting up a quantitative XRF system in the laboratory with the development of a in-house software routines.

Likewise the response characteristics of CdTe XR-100T detector and the efficiency calculations are performed using the same gamma radioactive emitters. The experimental and theoretical efficiencies of the XR-100T were compared, and the difference in the efficiencies were shown along with the source of errors. Escape events originated in this detector were observed and discussed. A comparison between the two solid state semiconductor detectors, and the advantages and disadvantages for XRF applications were described. The present study details how efficiency calculations can be accomplished.

We presented an analysis of elemental content of three metallic samples carried out by means of a pyroelectric generator in combination with a CdTe energy dispersive detector. Similarly we performed the elemental analysis using a Si-Pin detector on standard reference materials. These results have been compared with the values obtained from another X-ray analysis system XMET 3000 TXV+, also based on a Si-Pin detector but with a silver X-ray source.

Future work would include an evaluation of the validity of results produced by the CdTe detector. As XRF is a powerful technique but with a series of subtle

details that here have been highlighted. The method has clear advantage, since it is non destructive and can be applied in metallurgy, the chemical industry, quality control and forensic investigations, among others.

# Bibliography

- [1] Dearnaley, G., Northrop, D., *Semiconductor Counters for Nuclear Radiations*, E.& F.N. Spon Limited, Reading, London, 1964.
- [2] Taylor, J. M., *Semiconductor Particle Detectors*, Butterworths Inc., Reading, Washington, 1963.
- [3] Ouseph, P. J., *Introduction to Nuclear Radiation Detectors*, Plenum Press., Reading, New York, 1975.
- [4] Nicholson, P. W., *Nuclear Electronics*, John Wiley & Sons., Reading, 1974.
- [5] William Price, J., *Nuclear Radiation Detection*, McGraw-Hill, 1964.
- [6] Beiser, A. , *Concepts of Modern Physics*, McGraw Hill, 2003.
- [7] Auger, P., “Etude experimentale des directions d’emission des photoelectrons”, J. de Phys. et le Radium, 8(2) pp.85, 1927.



- [8] Jenkins, R., “X-ray Techniques : Overview”, *Encyclopedia in Analytical Chemistry*, pp. 13269-13288, John Wiley & Sons Ltd, 2000.
- [9] Castro-Colin, M., Lopez, J. A., Valaparla, S. K., “Elemental identification by X-ray fluorescence using a portable pyroelectric generator and a CdTe detector for an advanced laboratory course”, Book Chapter, Ed. A. Barranon, World Scientific, 2009.
- [10] René Van Grieken, E., Andrzej Markowicz A., *Handbook of X-ray Spectrometry*, Marcel Dekker Inc., New York, 2001.
- [11] Gordon Gilmore, R., *Practical Gamma-ray Spectrometry*, 2nd edition, John Wiley & Sons., Reading, 2008.
- [12] Mizota, H., Nakanishi, Y. Oohashi, H., Ito, Y., Tochio, T., Yoshikado, S., and Tanaka, T., “X-ray emission from  $LiTaO_3$  induced by thermal charges and structure analysis”, *Radiation Physics and Chemistry*, vol.75 pp.1626-1629, 2006.
- [13] <http://www.amptek.com/products.html>
- [14] Ida, H. and Kawai, J. “Portable x-ray fluorescence spectrometer with a pyroelectric x-ray generator”, *X-ray Spectrometry*, vol.34, pp. 225-229, 2005.

- [15] Kawai, J., Ida, H., Murakami, H., and Koyama, T., “X-ray Fluorescence analysis with a pyroelectric x-ray generator”, *X-ray Spectrometry*, vol.34, pp.521-524, 2005.
- [16] D. Karamanis, “Efficiency simulation of HPGe and Si(Li) detectors in  $\gamma$  and X-ray spectroscopy”, *Nucl. Instrum. Methods*, vol.A505, pp. 282-285, 2003.
- [17] Hull, E. L., Pehl, R. H., Tindall, C., Luke, P. N., and Kurfess, J. D. “Radiation Damage and charge collection effects in Si(Li) gamma ray detectors”, *Nucl. Instrum. Methods*, vol.A496, pp.123-128, 2003.
- [18] Keith, H. D. and Loomis, T.C., “Calibration and Use of a Lithium-drifted Silicon Detector for accurate analysis of X-ray Spectra”, *X-ray Spectrometry*, vol.5, pp.93-103, 1976.
- [19] Cox, C. E., Fisher, D. A., Schwarz, W. G., and Song, Y., “Improvement in the low energy collection efficiency of Si(Li) X-ray detectors”, *Nucl. Instrum. Methods*, vol.B241, pp.436-440, 2005.
- [20] Yalcin, P. Sulun, A., Bastug, A., Kurucu, Y., and Sahin, Y. , “The efficiency determination for Si(Li) Detector in the 3-723 keV energy range”,

- Canadian Journal of Analytical Sciences and Spectroscopy*, vol.50, No.3, 2005.
- [21] Cipolla, S. J., Milone, J. A. , “Methodological effects in Si(Li) detector efficiency calibrations”, *Nucl. Instrum. Methods*, vol.A505, pp.273-276, 2003.
- [22] Yunoki, A., Yamada, T., Sato, Y., Kawada, Y., Hino., Y., “Calibration of  $^{55}\text{Fe}$  activity with a lithium-drifted silicon detector”, *Applied Radiation and Isotopes*, vol.66, pp. 756-759, 2008.
- [23] Papp, T. and Campbell., J. L., “Size and origin of the escape peak in various Si(Li) detectors”, *X-ray Spectrometry*, vol.30, pp.77-82, 2001.
- [24] Fletcher., G., *Introduction to Mathematical Methods in Physics*, Wm. C. Brown Publishers., 1994.
- [25] Verger, L., Bonnefoy, J. P., Glasser, F., and Ouvrier, P., “New Developments in CdTe and CdZnTe Detectors for X and  $\gamma$  ray applications”, *Journal of Electronic Materials*, vol.26, No.6, 1997.
- [26] Redus, R. H., “Charge trapping in XR-100T CdTe and CZT Detectors”, Amptek Application Note(ANCZT-2 Rev.3).

- [27] Plagnard, J., Bobin, C., and Lepy, M.-C., “Accurate efficiency calibration of a low energy HPGe detector using a monochromatic x-ray source”, *X-ray Spectrometry*, vol.36, pp.191-198, 2007.
- [28] Eggert, T., Bosalu, O., Kemmer, J., Pahlke, A., and Wiest., F., “The spectral response of silicon X-ray detectors”, *Nucl. Instrum. Methods.*, vol.A568, pp.1-11, 2006.
- [29] Mohanty, B.P., Balouria, P., and Garg, M.L., “Comparison of experimental and theoretical efficiency of HPGe X-ray Detector”, *Nucl. Intsrum. Methods*, vol.A584, pp.186-190, 2008.
- [30] Sole, V. A., Papillon, E., Cotte, M., Walter, Ph., and Susini., J., “A multiplatform code for the analysis of energy-dispersive X-ray fluorescence spectra”, *Spectrochimica Acta*, part.B62, pp.63-68, 2007.
- [31] Lepy., M.-C., Campbell., J. L., Laborie, J. M., Plagnard, J., Stemmler, P., Teesdale., W. J., “Experimental Study of the response of semiconductor detectors to low energy photons”, *Nucl. Instrum. Methods.*, vol.A439, pp.239-246, 2000.
- [32] Szaloki, I., Szegedi, S., Varga, K., Braun, M., Osan, J., and Van Grieken, R., “Efficiency calibration of energy-dispersive detectors for application

- in quantitative x- and  $\gamma$ -ray spectrometry”, *X-ray Spectrometry*, vol.30, pp.49-55, 2001.
- [33] Loupilov, A., Sokolov, A., and Gostilo, V., “X-ray Peltier cooled detectors for X-ray fluorescence analysis” *Radiation Physics and Chemistry*, vol.61, pp.463-464, 2001.
- [34] Sokolov, A., Loupilov, A., and Gostilo, V., “Semiconductor Peltier cooled detectors for x-ray fluorescence analysis”, *X-ray Spectrometry*, vol.33, pp.462-465, 2004.
- [35] Scholze, F. and Procop, M., “Detection Efficiency of energy-dispersive detectors with low-energy windows”, *X-ray Spectrometry*, vol.34, pp.473-476, 2005.
- [36] Verma, H.R., “Efficiency Calibration of Si(Li) and HPGe detectors in the energy range of 5-60keV”, *Pramana- J.Phys.*, vol.25, No.5, pp.565-569, 1985.
- [37] Mesradi, M., Elanique, A., Nouredine, A., Pape, A., Raiser, D., Sellam, A., “Experimental Characterization and Monte Carlo Simulation of Si(Li) detector efficiency by radioactive sources and PIXE”, *Applied Radiation and Isotopes*, vol.66, pp.780-785, 2008.

- [38] Devan, K.R.S., Winkoun, D.P., and Murty, V.R.K., “Elemental Analysis using Radioisotope Excited X-ray Fluorescence”. *Appl. Radiat. Isot.*, vol.48, No.10-12, pp.1397-1401, 1997.
- [39] Bennal, A.S., Shidling, P.d., Badiger, N. M., Thontadarya, S.R., and Hanumaiah, B., “Measurements of K X-ray fluoescence analysis”, *Am. J. Phys.*, 73(9) pp.883 (2005).
- [40] Dasgupta, M., Sharma, B.k., Ahuja, B.L., and Mohammad, F.M., “Some experiments on X-ray Flourescence for the student labaratory”, *Am. J. Phys.*, 56(3) pp.245 (1988).
- [41] Brownridge, J.D., “Pyroelectric X-ray Generator”, *Nature*, 358(6384) pp.287,1992.
- [42] Brownridge, J.D. and Raboy, S., “Investigations of pyroelectric generation of x rays”, *J. Appl. Phys.*, 86(1) pp.640 (1999).
- [43] Jenkins, R., Manne, R., Robins, R., and Senemaud, C., “Nomenclature system for X-ray Spectroscopy”, *Pure and Appl. Chem.*, 63(5) pp.735 (1991).
- [44] Kortright, J.B. and Thompson, A.C., “X-ray emission energies in X-ray Data Booklet”, (Ed. by A.C. Thompson and D.Vaughan, Lawrence Berke-

ley National Laboratory, Riverside, CA, USA, 2nd edition., 2001), pp.1.2-1.27.

[45] Sherman, J., “The Theoretical derivation of fluorescent X-ray intensities from mixtures”, *Spectrochimica Acta.*, vol.7, pp.283-306, 1955.

[46] Rousseau., R. M., “Some considerations on how to solve the Sherman equation in practice”, *Spectrochimica Acta.*, Part B, pp.1491-1502, 2004.

[47] <http://www.xcom.com>

# Appendix A

## Technical Specifications

### A.1 COOL-X

Table A.1: COOL-X technical specifications.

Miniature Size	15-mm diam * 10-mm
Low power	< 300 mW
Battery	9 V Standard Battery
Variable End Point Energy	up to 35 kV
Peak x-ray flux	$10^8$ photons per second
Solid State	Pyroelectric crystal



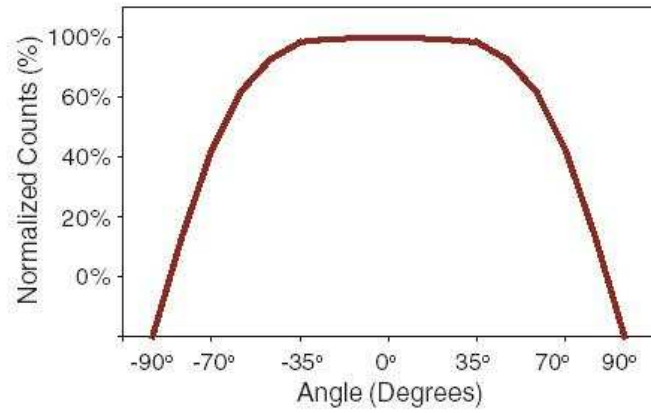


Figure A.1: Cool-X Output flux vs angle [13].

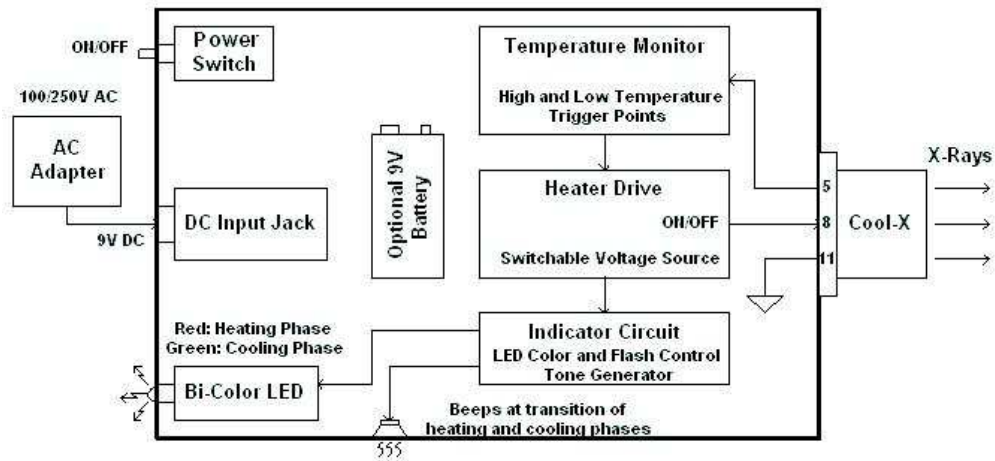


Figure A.2: Cool-X Controller System [13].

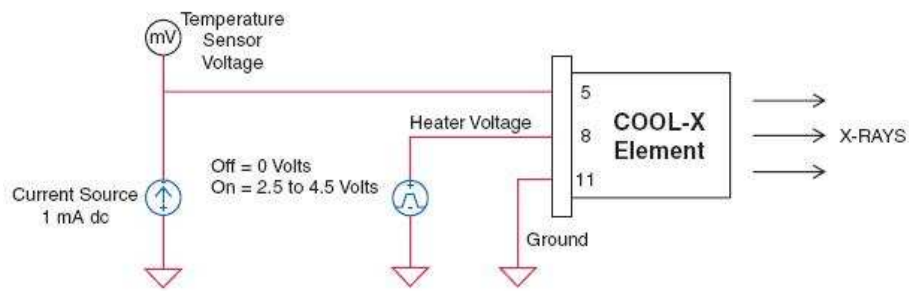


Figure A.3: Cool-X operation from 2.5 to 4.5 V DC supply [13].

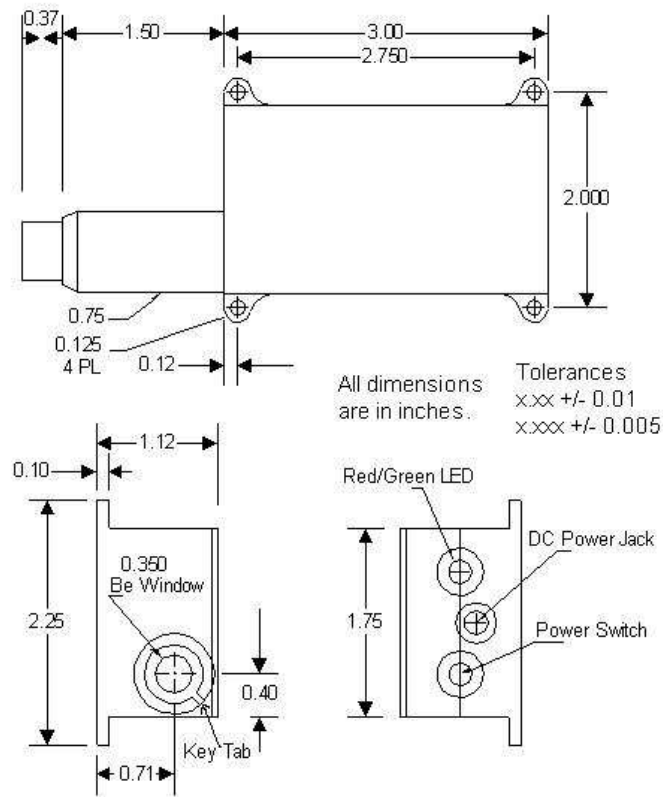


Figure A.4: Cool-X Mechanical Dimensions [13].

## A.2 XR-100CR

Table A.2: XR-100CR technical specifications.

Detector Type	Si-Pin
Detector Size	13 mm <sup>2</sup>
Silicon Thickness	300 $\mu$ m
Energy Resolution @ 5.9 keV	219 eV FWHM
Detector Be window thickness	1 mil (25 $\mu$ m)
Power	< 1 Watt
Operating conditions	0°C to +40°C

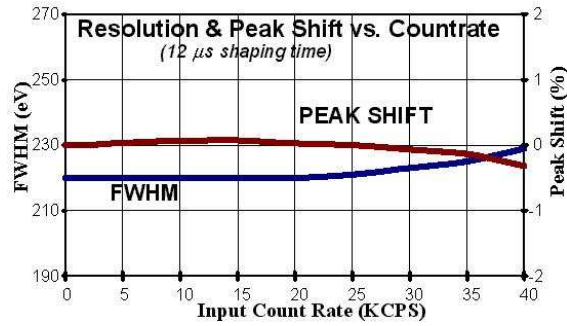


Figure A.5: Resolution and Peak Shift vs. Count Rate [13].

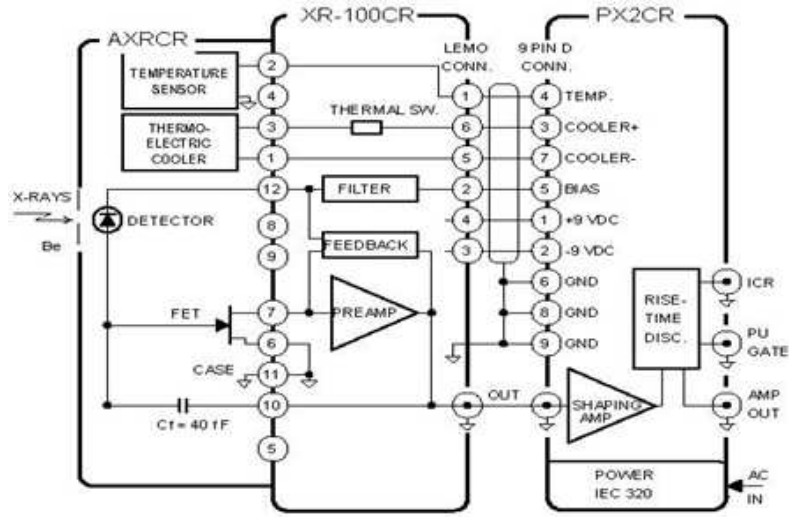


Figure A.6: XR-100CR Connection Diagram [13].

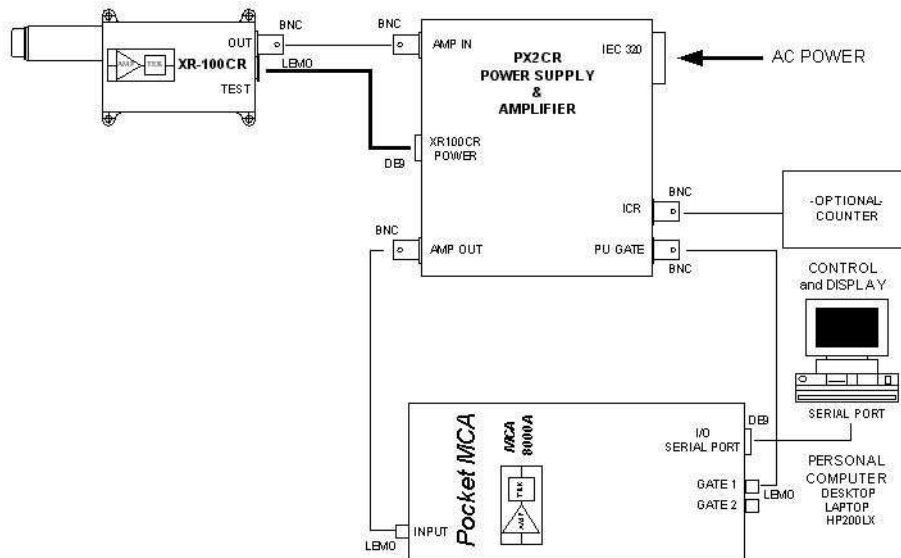


Figure A.7: XR100CR, PX2CR, MCA8000A connection diagram [13].

### A.3 XR-100T-CdTe

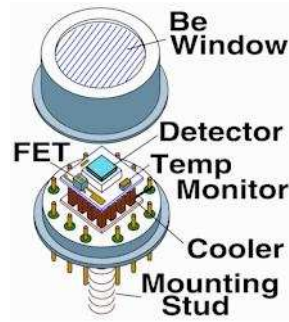


Figure A.8: XR100T-CdTe Detector [13].

Table A.3: XR-100T-CdTe Specifications.

Detector Type	Cadmium Telluride (CdTe) Diode
Detector Size	$7 \text{ mm}^2$
Detector Thickness	1 mm
Energy Resolution @ 122 keV	$< 1.2 \text{ keV FWHM}$
Detector Be window thickness	1 mil ( $25 \text{ }\mu\text{m}$ )
Power	$< 1 \text{ watt}$
Operating conditions	$0^\circ\text{C}$ to $+40^\circ\text{C}$

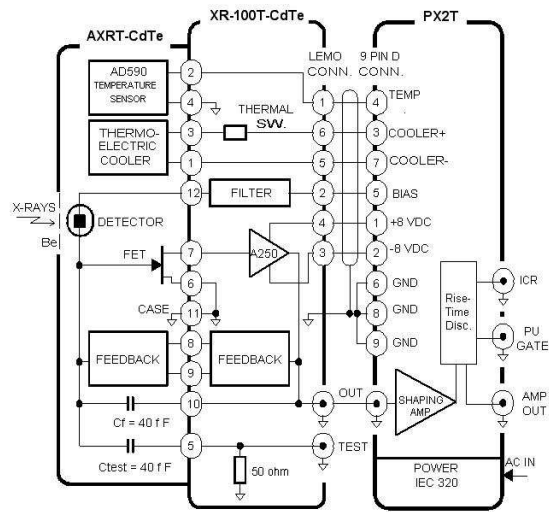


Figure A.9: XR100T-CdTe Connection Diagram [13].

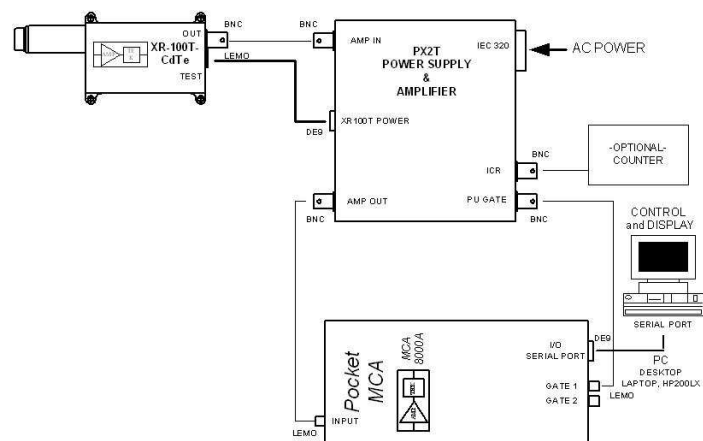


Figure A.10: XR100T-CdTe, PX2T, and MCA8000A Connection Diagram [13].

## A.4 MCA8000A

Features [13]:

- 16K Data Channels
- Conversion time  $< 5 \mu s$  ( $> 200,000$  cps)
- Differential non-linearity  $< \pm 0.6\%$
- Integral nonlinearity  $< \pm 0.02\%$
- Dimensions : 6.5 x 2.8 x 0.8 in / 165 x 71 x 20 mm
- PC software supports ROI, energy calibration, peak information, MCA configuration, and file management



Figure A.11: MCA8000A Pocket multichannel analyzer [13].

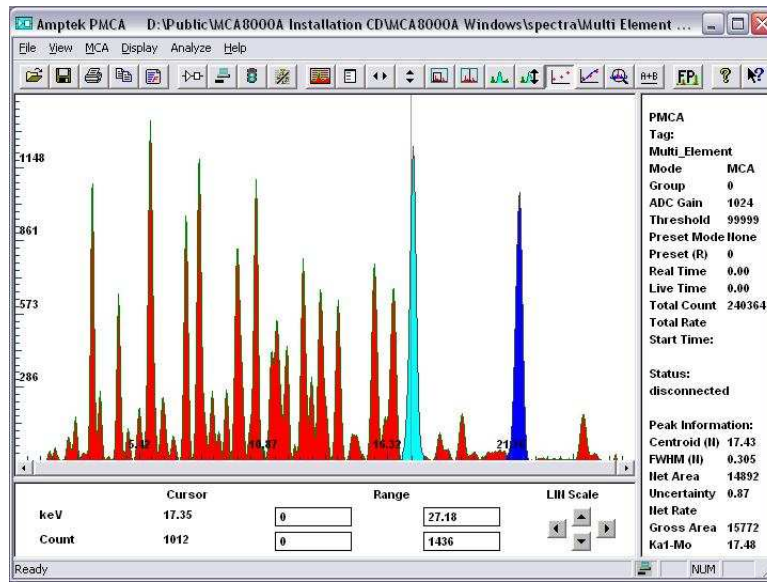


Figure A.12: ADMCA Windows Software showing ROI [13].

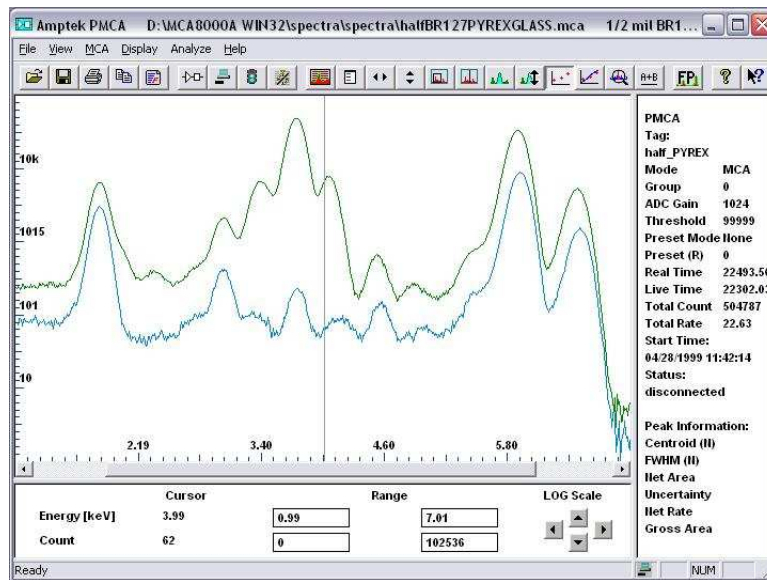


Figure A.13: ADMCA Windows Software showing multiple spectra capability [13].



The ADMCA Software allows data acquisition and display on any PC compatible computer. This software supports region of interest (ROI), energy calibration, peak search, peak information, MCA8000A configuration, multiple spectra, and mathematical operations. Automatic peak search is possible with a routine that marks the identified peaks as ROIs. Peak counts and FWHM can be automatically calculated and displayed in either channels or user-defined calibration units.

The software includes an isotope library and listing of atomic x-ray emission lines. The peak information panel automatically suggests the isotope or x-ray line closest to the peak. Multiple spectra can be displayed at the same time and mathematical operations can be performed on the spectra. Examples of the Windows software are shown in Figures A.12 and A.13.

## **A.5 XMET 3000 TXV+**

The XMET 3000 TXV+ is a rugged, hand held XRF analyzer which incorporates a modern x-ray tube. The XMET alloy analyzer provides a fast and simple way to perform alloy analysis in a fairly versatile way: in the field, inside the laboratory or in production facilities. Measurements with the XMET can be performed in the Fundamental Parameters or Empirical Assay modes.

Table A.4: XMET 3000 TXV+ Specifications.

Analysis Range	From Ti to U
Display	320 * 240 dpi
Battery	2 Li-ion
Battery charger	240/110 V - 50-60 Hz
Detector	High-res. Peltier cooled Si-Pin
X-ray tube	Max Voltage 40 kV - Ag target
User Interface	PDA/Windows CE OS (Alloy Analysis software)
Dimensions	9.9cm(W) * 28.3cm(L) * 27.8cm(H)
Operating conditions	-10°C to +50°C

# Appendix B

## PyMca Software

The setup of the configuration parameters of the fit had to be as simple as possible. This practical requirement led to the development of a complete visualization and data analysis tool named PyMCA, Python MultiChannel Analyzer [30]. This application relies on Python bindings of a C++ programming toolkit. The fitting code can run in prompt or batch mode fully independent of any graphical package.

## B.1 Algorithms

### B.1.1 Peak shape model

A Gaussian peak is characterized by three parameters: the position, width, and height or area. It is desirable to describe the peak in terms of its area rather than its height because the area is directly related to the number of X-ray photons detected. The first approximation to the profile of a single peak is then given by:

$$\frac{A}{s\sqrt{2\pi}} \exp \left[ \frac{-(x_i - x_o)^2}{2s^2} \right], \quad (\text{B.1})$$

where  $A$  is the peak area [counts],  $s$  is the width of the Gaussian [channels] or [eV] and  $x_o$  the location of the peak maximum [channels] or [eV]. The FWHM is related to  $s$  by  $\text{FWHM} = 2.3548 s$ .

### B.1.2 FWHM and peak positions

The energies of the X-ray fluorescence lines are typically known with an accuracy of 1 eV or better. The pattern of peaks observed in the spectrum is directly related to the elements present in the sample. Based on these elements we can predict all of the X-ray lines that constitute the spectrum and their energies.

The peak fitting function is therefore written in terms of energy rather than channel number. Defining ZERO as the energy of channel 0 and expressing the spectrum GAIN in eV/channel, the energy of channel  $i$  is given by:

$$E(i) = ZERO + GAIN \times i, \quad (\text{B.2})$$

and the normalized Gaussian peak can be written as:

$$G(i, E_j) = \frac{GAIN}{s\sqrt{2\pi}} \exp \left[ \frac{-(E_j - E(i))^2}{2s^2} \right], \quad (\text{B.3})$$

with  $E_j$  the energy of the x-ray line and  $s$  the peak width given by:

$$s^2 = \left( \frac{NOISE}{2.3548} \right)^2 + 3.85 \times FANO \times E_j, \quad (\text{B.4})$$

In this equation, NOISE is the electronic contribution to the peak width, typically 80-100 eV FWHM, FANO is the Fano factor,  $\approx 0.114$  for Si, and 3.85 eV the energy required to produce an electron-hole pair in silicon. The non-linear least-squares fit optimizes ZERO, GAIN, NOISE and FANO for the entire fitting region. The actual position and width of the peaks are calculated using the Eqs. B.2, B.3, and B.4.

### B.1.3 Element line groups

The spectrum of an element can be represented by [45, 46]:

$$y_p(i) = A \sum_{j=1}^{N_p} R_j G(i, E_j), \quad (\text{B.5})$$

where  $G$  are the Gaussians for the various lines of  $E_j$  energy and  $R_j$  the relative intensities of the lines. The summation runs over all lines in the group ( $N_p$ ) with  $\sum R_j = 1$ . The transition probabilities of all lines originating from a vacancy in the same (sub-)shell ( $K, L_1, L_2 \dots$ ) are constant, independent of the excitation. However, the relative intensities depend on the absorption in the sample and the detector windows. To take this into account, the X-ray attenuation must be included in Eq. B.5.

The relative intensity ratios are obtained by multiplying the transition probabilities by an absorption correction term [45, 46]:

$$R'_j = \frac{R_j T_A(E_j) [1 - T_D(E_j)]}{\sum R_j T_A(E_j) [1 - T_D(E_j)]}, \quad (\text{B.6})$$

The absorption correction term  $T_A(E)$ , used in the Eq. B.6, includes the X-ray attenuation in all layers and windows between the sample surface and the active area of the detector while the term,  $[1 - T_D(E)]$ , accounts for the possibility of the photon to go through the detector without interacting, it is a

transmission coefficient.

If a sample composition is given, the program uses a parallel beam approximation taking  $R_j'' = R_j' / \sum R_j'$  with [45, 46]:

$$R_j' = \frac{\omega_j P_j(E_0) R_j T_A(E_j) [1 - T_D(E_j)]}{\mu_T(E_0) + \mu_T(E_j) \frac{\sin \psi_1}{\sin \psi_2}} \times \left[ 1 - e^{\left[ \left( \frac{\mu_T(E_0)}{\sin \psi_1} \right) + \left( \frac{\mu_T(E_j)}{\sin \psi_2} \right) \right] \rho d} \right], \quad (\text{B.7})$$

where  $\omega_j$  is the fluorescence yield of the shell being considered,  $P_j$  takes into account the possibility to have a vacancy in the  $j$  shell,  $\mu_T$  is the total mass attenuation coefficient of the sample,  $E_0$  is the incident photon beam energy,  $\psi_1$  and  $\psi_2$  are the angles of the incoming and fluorescent beam respect to the sample surface,  $\rho$  is the sample density and  $d$  is the sample thickness. The above formulae had to be adapted to the case of an incoming beam presenting a set of discrete energies in order to account for harmonic contamination [45, 46]. The approach can also be applied to polychromatic sources, provided they are modeled by a set of discrete energies.

Considering the excitation beam as composed of photons of energies  $E_{0k}$  with a relative rate  $w_k$ , we can generalize Eq. B.7 as

$$R_j' = \sum \frac{\omega_k T_A(E_{0k}) \omega_j P_j(E_{0k}) R_j T_A(E_j) [1 - T_D(E_j)]}{\mu_T(E_{0k}) + \mu_T(E_j) \frac{\sin \psi_1}{\sin \psi_2}}$$

$$\times [1 - \exp [(\frac{\mu_T(E_{0k})}{\sin \psi_1}) + (\frac{\mu_T(E_j)}{\sin \psi_2})] \rho d],$$

where the dependency on the incident photon energies has been explicitly shown. The term  $T_A(E_{0k})$  has been introduced in order to show that the program takes into account the different attenuation of the incoming photons in their path to the sample, while the other equations remain valid provided  $E_0$  is replaced by  $E_{0k}$ , [45, 46, 30].

#### B.1.4 Sum and escape peaks

The escape fraction  $f$  is defined as the number of counts in the escape peak  $N_e$  divided by the number of detected counts, escape plus parent. PyMCA assumes normal incidence to the detector and considers escape only from the front surface [30]. The area of the escape peak, relative to the area of the parent peak can be calculated from the escape fraction [30]:

$$\eta = \frac{N_e}{N_p} = \frac{f}{1 - f}, \quad (\text{B.8})$$

For a Si detector, the escape peaks can be modeled by a Gaussian at energy 1.742 keV below the parent peak. Including the escape peaks, the description of the fluorescence of element becomes [30]:



$$y_p(i) = A \sum_{j=1}^{N_p} R'_j [G(i, E_j) + \eta G(i, E_j - E_{esc})], \quad (\text{B.9})$$

where  $G$  represents the Gaussian fitting function and  $E_{esc}$  the energy of the escaped photon. For each  $E_j$ , PyMCA calculates all the detector fluorescent lines that can be originated and applies the formulae to each of them and this implementation automatically takes into account L shell escape lines. In order to limit the number of escape lines, the user can specify the maximum number of individual escape lines per  $E_j$  to be considered.

## B.2 Theoretical database

The program [30] uses by default a built-in database in which, instead of using emission energies, it derives the emission energies from the binding energies of Larkins. The K shell fluorescence yields are taken from Bambynek's formula. The K shell radiative emission probabilities are taken from Scofield's Dirac-Fock calculations. The L shell fluorescence yields, Coster-Kronig data and the L shell radiative transition probabilities are from Scofield's Dirac-Hartree-Slater work. For elements where theoretical data are missing, the needed values are calculated by interpolation. Mass attenuation coefficients are log-log interpolated into ASCII tables previously generated by XCOM [47].

The expected count rate of an element group of lines can be written as [30]:

$$A = I_0 C \frac{\Omega}{4\pi} \sum R_j'', \quad (\text{B.10})$$

where  $I_0$  is the incident beam rate,  $C$  is the mass fraction of the element in the sample and  $\Omega/4\pi$  represents the detector geometric efficiency. Measured the areas  $A$ , the only unknown terms to calculate the mass concentrations are the incident photon flux and the detector efficiency. These parameters are given by the user, either directly or indirectly, asking the program to take one of the matrix elements as internal reference. PyMCA [30] implements most of the needs of X-ray fluorescence spectroscopy. It has several unique features as the implementation of energy dependent photoelectric cross sections and a complete description of the M shell. It can process batches of thousands of spectra.

# Appendix C

## Standard Reference Materials

The Standard Reference Materials (SRM) used in this work are certified by the National Institute of Standards and Technology (NIST). A NIST-certified value is a value for which NIST has the highest confidence in its accuracy. Values of elemental content are reported as mass fractions/weight. The certified values for the three SRM's are given below in their respective tables.

Table C.1: SRM Specifications.

SRM	Diameter	Thickness
1240C	6.3cm	1.9cm
C2417	50mm (2in.)	16mm (5/8in.)
1159	3.1cm (5/4in.)	1.9cm (3/4in.)

Table C.2: Certified Values for SRM 1240c Aluminum Alloy 3004.

Constituent	Value (mass fraction %)	Expanded Uncertainty (mass fraction %)	Expansion Factor, K
Si	0.1804	0.0038	2.3
Fe	0.501	0.016	2.0
Cu	0.1484	0.0054	2.0
Mn	1.268	0.014	2.0
Mg	1.110	0.021	2.0
Ni	0.00434	0.0008	2.0
Zn	0.0514	0.0011	2.0
V	0.01850	0.00057	2.0
Ga	0.0181	0.0015	2.0
Ti	0.0218	0.0015	2.0

Table C.3: Certified Values for SRM 1159 EM Alloy.

Element	Percent by Weight
Carbon	0.007
Copper	0.038
Chromium	0.06
Phosphorous	0.003
Cobalt	0.022
Iron	51.0
Manganese	0.30
Nickel	48.2
Sulfur	0.003
Silicon	0.32
Molybdenum	0.01

Table C.4: Certified Values for SRM C2417 Lead base Alloy.

Element	Percent by Weight
Antimony	0.010
Bismuth	0.011
Arsenic	0.010
Copper	0.010
Silver	0.010
Uncertified Elements	Percent by weight
Aluminum	<0.0001
Cadmium	<0.0002
Calcium	<0.001
Cobalt	<0.0002
Iron	<0.0003
Manganese	<0.0003
Nickel	<0.0005
Sulfur	<0.0005
Zinc	<0.0005

## Curriculum Vitae

S. K. Valaparla obtained a B. E. in Electrical and Electronics Engineering at Andhra University, India, under the advice of Dr. Govardhana Rao R., on the topic of “Power System Transient Stability Enhancement Using Thyristor Controlled Series Compensator”. At UTEP he has been interested in understanding the physics of radiation, mainly the interactions of X-ray photons with matter. During his work at UTEP he constructed a small setup to carry out XRF analysis, and part of its characterization is discussed in the present work. Recently he has extended his interest in radiation to the field of Medical Physics and plans to pursue Ph.D. studies in that area.

Permanent address:      1201 Randolph Drive, Apt:340  
El Paso, Texas 79902

This thesis was typed by Sunil K. Valaparla.